SIAM J. IMAGING SCIENCES
Vol. 1, No. 1, pp. 75–114
© 2008 Society for Industrial and Applied Mathematics

Edge Illumination and Imaging of Extended Reflectors*

Liliana Borcea†, George Papanicolaou‡, and Fernando Guevara Vasquez§

Abstract. We use the singular value decomposition of the array response matrix, frequency by frequency, to image selectively the edges of extended reflectors in a homogeneous medium. We show with numerical simulations in an ultrasound regime, and analytically in the Fraunhofer diffraction regime, that information about the edges is contained in the singular vectors for singular values that are intermediate between the large ones and zero. These transition singular vectors beamform selectively from the array onto the edges of the reflector cross-section facing the array, so that these edges are enhanced in imaging with travel-time migration. Moreover, the illumination with the transition singular vectors is done from the sources at the edges of the array. The theoretical analysis in the Fraunhofer regime shows that the singular values transition to zero at the index $N^\star(\omega) = |\mathcal{A}||\mathcal{B}|/(\lambda L)^2$. Here $|\mathcal{A}|$ and $|\mathcal{B}|$ are the areas of the array and the reflector cross-section, respectively, ω is the frequency, λ is the wavelength, and L is the range. Since $(\lambda L)^2/|\mathcal{A}|$ is the area of the focal spot size at range L, we see that $N^\star(\omega)$ is the number of focal spots contained in the reflector cross-section. The ultrasound simulations are in an extended Fraunhofer regime. The simulation results are, however, qualitatively similar to those obtained theoretically in the Fraunhofer regime. The numerical simulations indicate, in addition, that the subspaces spanned by the transition singular vectors are robust with respect to additive noise when the array has a large number of elements.

Key words. broadband array imaging, travel-time migration, selective illumination, singular value decomposition, generalized prolate spheroidal wave functions

AMS subject classifications. 35R30, 78A46

DOI. 10.1137/07069290X

1. Introduction.

Accurate array imaging of extended reflectors requires information that comes from their edges. However, such information is masked by the strong reflections received from the body of the reflectors. The singular value decomposition (SVD) of the array impulse response matrix $\widehat{\Pi}(\omega)$, at frequency ω, is a natural tool for filtering strong reflections and concentrating on the weaker edge effects. Here $\widehat{\Pi}(\omega)$ is the complex matrix with entries $\widehat{\Pi}(\vec{\mathbf{x}}_r, \vec{\mathbf{x}}_s, \omega)$, which are the Fourier transforms of the time traces $\Pi(\vec{\mathbf{x}}_r, \vec{\mathbf{x}}_s, t)$ recorded at receiver locations $\vec{\mathbf{x}}_r$ in the array when the source at $\vec{\mathbf{x}}_s$ emits an impulse with flat spectrum over the bandwidth.

*Received by the editors May 25, 2007; accepted for publication (in revised form) December 11, 2007; published electronically March 20, 2008.

http://www.siam.org/journals/siims/1-1/69290.html

†Computational and Applied Mathematics Department, Rice University MS134, 6100 Main St., Houston, TX 77005 (borcea@camm.rice.edu). This author's work was partially supported by the Office of Naval Research, under grant N00014-05-1-0699 and by National Science Foundation grants DMS-0604008, DMS-0305056, DMS-0354658.

‡Department of Mathematics, Stanford University, 450 Serra Mall Bldg. 380, Stanford, CA 94305 (papanico@math.stanford.edu). This author's work was supported by grants NSF-DMS-0354674-001, ONR-N00014-02-1-0088, and 02-SC-ARO-1067-MOD-1.

§Department of Mathematics, University of Utah, 155 S 1400 E, Rm 233, Salt Lake City, UT 84112-0090 (fguevara@math.utah.edu). This author's work was supported by grants NSF-DMS-0354674-001, ONR-N00014-02-1-0088, and 02-SC-ARO-1067-MOD-1.

We carry out a theoretical analysis of the SVD of $\widehat{\Pi}(\omega)$ in the Fraunhofer regime, in which the Fresnel number [8, Chapter 8.2]

$$\frac{a^2}{\lambda L} = \frac{a}{(\lambda L)/a} \tag{1.1}$$

is large. Here a is the linear array size, λ is the wavelength, and L is the range. The Fresnel number is the ratio of a to the focal spot size $(\lambda L)/a$, which is the first zero of the array diffraction pattern in the Fraunhofer regime [8, Chapter 8.5]. In this regime the SVD of the array response matrix can be obtained using the generalized prolate spheroidal wave functions [38, 29, 41, 5]. This is because the SVD analysis can be reduced by factorization of the response matrix $\widehat{\Pi}(\omega)$ to the eigenvalue problem of a self-adjoint operator of a special form, as explained in section 4.4.

In the Fraunhofer regime, we show that if b is a linear cross-range size of the reflector, then $b^2a^2/(\lambda L)^2$ is approximately the number $N^\star(\omega)$ of nonzero singular values. This says that the effective rank of $\widehat{\Pi}(\omega)$ is determined by the number of focal spots of area $(\lambda L/a)^2$ that fit inside a reflector of area b^2, a fact that has been observed empirically in [44, 43] and which we justify here theoretically.

Beyond the threshold index $N^\star(\omega)$, the singular values transition rapidly to zero. The right singular vectors associated with the transition singular values correspond to illuminations from the edges of the array. The travel-time images with these illuminations focus selectively on the edges of the reflector cross-section facing the array. The edges of the reflector can thus be emphasized in travel-time migration images. This fact was also shown with variational methods in the Fraunhofer regime in [5] and has been observed experimentally in [26].

The Fraunhofer regime arises naturally in optics [8, Chapter 8.5]. In ultrasonic array imaging applications we encounter an extended Fraunhofer regime, in which edge diffraction effects play a more prominent role. The Fraunhofer regime is based on the assumption that $b \ll a$, so that the phase of the free space Green's function

$$\widehat{G}_0(\vec{\mathbf{x}}, \vec{\mathbf{y}}, \omega) = \frac{\exp[ik\,|\vec{\mathbf{x}} - \vec{\mathbf{y}}|]}{4\pi\,|\vec{\mathbf{x}} - \vec{\mathbf{y}}|} \tag{1.2}$$

can be linearized with respect to points $\vec{\mathbf{y}}$ in the reflector. This reduces the mathematical analysis to that of Fourier integral operators. In the extended Fraunhofer regime the reflector is large ($b \sim a$), and the phase of the Green's function contains the quadratic Fresnel term in $\vec{\mathbf{y}}$ that accounts for stronger diffraction effects. This Fresnel term complicates the SVD analysis of $\widehat{\Pi}(\omega)$, because the problem does not reduce as in the Fraunhofer case to the spectral decomposition of a self-adjoint, compact operator (see section 5). However, we show here with numerical simulations that the behavior of the singular values and singular vectors is qualitatively similar to that of the Fraunhofer regime. We also demonstrate the effectiveness of the SVD for edge illumination and its robustness to additive noise when the array has a large number of transducers. Numerical simulations in the Fraunhofer regime are computationally demanding because wavelengths are typically very small compared to the size of the array and the reflector. We do not carry out numerical simulations in the Fraunhofer regime.

The basic imaging function used in this paper is travel-time migration. It is easy to implement, it is not demanding computationally, and it is widely used in several applied areas such

as seismic imaging [9, 10, 3, 2], radar imaging [15, 7], and nondestructive evaluation of materials [34]. There are, of course, more accurate broadband imaging methods such as full wave migration [2, Chapter 4] and full least squares inversion [2, Chapter 9]. Single frequency least squares techniques that estimate the support of the reflector using level sets (shape derivatives) [37, 16, 21] also work well when the array is large and the signal-to-noise ratio (SNR) of the array data is high. However, these methods are more demanding computationally. In this paper (see also [5]) we point out that migration becomes more efficient, accurate, and robust when coupled with a data filtering process that tends to emphasize the echoes from the edges of the reflectors. The data filtering increases the computational complexity of the migration method, because the filters are defined frequency by frequency with the SVD of the response matrix $\widehat{\Pi}(\omega)$, as explained in section 2.2.

The SVD can also be used in imaging with the linear sampling method [13, 14, 11, 12]. In this approach, the measurements are made on a sphere of very large (asymptotically infinite) radius R surrounding the reflector, and the image is formed with the SVD of the far field operator with kernel $\mathcal{S}_\omega(\vec{\theta}_r, \vec{\theta}_s)$. With the data acquisition geometry considered in [13, 14, 11, 12], $\mathcal{S}_\omega$ is related to the response matrix $\widehat{\Pi}(\omega)$ by

$$\mathcal{S}_\omega(\vec{\theta}_r, \vec{\theta}_s) = \lim_{R\to\infty} R^2 e^{-2ikR} \widehat{\Pi}(R\vec{\theta}_r, R\vec{\theta}_s, \omega).$$

Here $k = \omega/c$ is the wavenumber, and $\vec{\theta}_s$ and $\vec{\theta}_r$ are unit vectors. The theoretical analysis of the linear sampling method deals with the full scattering problem, not only the Born approximation, and gives good results with high SNR data and with full aperture, where $\mathcal{S}_\omega(\vec{\theta}_r, \vec{\theta}_s)$ is measured in all directions $\vec{\theta}_r$ and $\vec{\theta}_s$. It is a single frequency method which does not appear to have a natural time-domain extension.

In this paper we use the SVD of the limited aperture ($a \ll L$) response matrix $\widehat{\Pi}(\omega)$ for all the frequencies in the bandwidth. We also make explicit the connection between the geometrical features of the reflector cross-section facing the array and the singular vectors of $\widehat{\Pi}(\omega)$ corresponding to the transition singular values whose indices are near the threshold $N^\star(\omega)$.

In the full aperture case the behavior of the singular values of the far field operator with kernel $\mathcal{S}_\omega$ is considered in [14, 11]. It is shown in particular, in [14, Chapter 4.3], that when the reflector is contained in a ball of fixed radius b, the singular values decay like $(ekb/(2n))^n$ as the index $n \to \infty$. The threshold index at which the singular values start to decay is not identified in [14, 11]. It is shown in [27, 28] that for two-dimensional disk-shaped reflectors of radius b the transition index $N^\star(\omega)$ is the integer part of kb. This threshold is then used in [27, 28] to characterize the convex scattering support associated with the data $\mathcal{S}_\omega(\vec{\theta}_r, \vec{\theta}_s)$ for a fixed incident direction $\vec{\theta}_s$ and all unit vectors $\vec{\theta}_r$. The convex scattering support is defined in [27, 28] as the smallest convex set that can produce the far field measurements. It is a subset of the convex hull of the support of any scatterer that gives the measured far field data. As shown in [22], the convex scattering support can also be determined from back-scattered, far field measurements $\mathcal{S}_\omega(\vec{\theta}, \vec{\theta})$, for all directions $\vec{\theta}$.

In [27, 28, 22] there is no discussion regarding the connection between the shape of the scatterer and the form of the singular functions of $\mathcal{S}_\omega$. In this paper we make this connection precise for array imaging in the Fraunhofer regime, in the Born approximation. We also use

it to define, in general, data filtering operators that emphasize the echoes from the edges in the time-domain data. The filtered data is then used in travel-time migration to obtain sharp images of the support of the reflectors. To assess the robustness of the conclusions drawn from the analysis, we present numerical simulations that account for multiple scattering (see section 3.2) and for strong diffraction effects (i.e., the extended Fraunhofer regime) (see section 5). We find that the theoretical results hold qualitatively in both cases.

We study the limited aperture problem $a \ll L$. The full aperture case, with measurements made all around the reflector, in the far field, as considered in [14, 11, 27, 28, 22] is very different. However, some ideas in this paper extend to the full aperture problem, as discussed briefly in Appendix C.

The paper is organized as follows. In section 2 we formulate the array imaging problem and the selected subspace migration imaging algorithm. In section 3 we present the results of numerical simulations using this algorithm in an ultrasonic imaging regime, including data with additive noise. In section 4 we introduce the Fraunhofer diffraction regime and analyze the structure of the SVD of the array response matrix. In section 5 we introduce and discuss an extended Fraunhofer regime that is closer to our ultrasonic imaging simulations than the Fraunhofer regime. We end with a summary and conclusions in section 6.

2. Array imaging.

We wish to image a reflective target with an active array $\mathcal{A}$ consisting of N_s emitters and N_r receivers. The data in the frequency domain is denoted by $\widehat{\Pi}(\omega) \in \mathbb{C}^{N_r \times N_s}$. It is the array impulse response matrix, assumed known in the frequency band $\omega_0 + [-B/2, B/2]$. Here ω_0 is the central frequency and B is the bandwidth. The entries $\widehat{\Pi}(\vec{\mathbf{x}}_r, \vec{\mathbf{x}}_s, \omega)$ of this matrix are the Fourier transforms of the time traces of the echoes received at $\vec{\mathbf{x}}_r \in \mathcal{A}$, when the source at $\vec{\mathbf{x}}_s \in \mathcal{A}$ (see Figure 1) emits the signal

$$g(t) = \exp[i\omega_0 t]\frac{\sin(Bt/2)}{\pi t}$$

whose Fourier transform is

$$\widehat{g}(\omega) = \int \exp[-i\omega t] g(t) dt = \begin{cases} 1 & \text{if } |\omega - \omega_0| \le B/2, \\ 0 & \text{otherwise.} \end{cases}$$

We assume for simplicity that the sources and receivers are collocated, which means that all array elements act as emitters and receivers and that $N_r = N_s = N$. We also assume that the reflector or target is immersed in a medium with constant wave speed c_0.

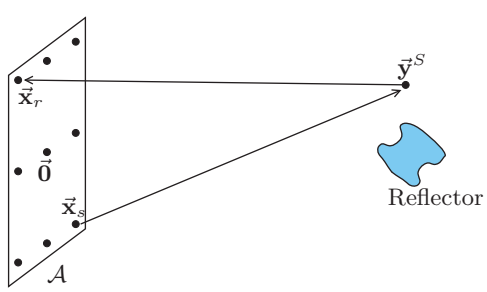

Figure 1. *General setup for array imaging.*

2.1. Travel-time migration. The Kirchhoff or travel-time migration function is given by [9, 10, 3, 2]

$$\mathcal{I}_{\mathrm{KM}}(\vec{\mathbf{y}}^S;\widehat{f}) = \int_{|\omega-\omega_0|\le B/2} d\omega \sum_{s=1}^{N}\sum_{r=1}^{N} \exp\left[i\omega\tau(\vec{\mathbf{x}}_r,\vec{\mathbf{y}}^S) + i\omega\tau(\vec{\mathbf{x}}_s,\vec{\mathbf{y}}^S)\right] \cdot \overline{\widehat{\Pi}(\vec{\mathbf{x}}_r,\vec{\mathbf{x}}_s,\omega)\widehat{f}(\vec{\mathbf{x}}_s,\omega)}. \tag{2.1}$$

Here $\tau(\vec{\mathbf{x}}_r,\vec{\mathbf{y}}^S)$ is travel time from the point $\vec{\mathbf{x}}_r$ to $\vec{\mathbf{y}}^S$, $\vec{\mathbf{y}}^S$ is a search point in the image domain, and the pulse sent from location $\vec{\mathbf{x}}_s$ is $\widehat{f}(\vec{\mathbf{x}}_s,\omega)$. Since the propagation medium is homogeneous, we have $\tau(\vec{\mathbf{x}}_r,\vec{\mathbf{y}}^S) = \left|\vec{\mathbf{x}}_r - \vec{\mathbf{y}}^S\right|/c_0$.

2.2. Selected subspace migration. We will use an imaging functional in which we replace the array data $\widehat{\Pi}(\omega)$ in (2.1) by a filtered version $D[\widehat{\Pi}(\omega);\omega]$:

$$\mathcal{I}_{\mathrm{SM}}(\vec{\mathbf{y}}^S;\widehat{f}) = \int_{|\omega-\omega_0|\le B/2} d\omega \sum_{s=1}^{N}\sum_{r=1}^{N} \exp\left[i\omega\tau(\vec{\mathbf{x}}_r,\vec{\mathbf{y}}^S) + i\omega\tau(\vec{\mathbf{x}}_s,\vec{\mathbf{y}}^S)\right] \cdot \overline{\left(D\left[\widehat{\Pi}(\omega);\omega\right]\right)_{r,s}\widehat{f}(\vec{\mathbf{x}}_s,\omega)}. \tag{2.2}$$

The filtering operator $D[\,\cdot\,;\omega] : \mathbb{C}^{N\times N} \to \mathbb{C}^{N\times N}$ acts only on the singular values of the response matrix. It has the form

$$D[\widehat{\Pi}(\omega);\omega] = \sum_{j=1}^{N} d_j(\omega)\sigma_j(\omega)\mathbf{u}_j(\omega)\mathbf{v}_j^*(\omega), \tag{2.3}$$

where the filter weights are $d_j(\omega) \ge 0$, $\mathbf{u}_j(\omega)$ and $\mathbf{v}_j(\omega)$ are the left and right singular vectors of the response matrix, respectively, and $\sigma_1(\omega) \ge \sigma_2(\omega), \ldots, \ge \sigma_N(\omega) \ge 0$ are its singular values. We recall that the singular vectors form two orthonormal bases, so that for $1 \le i \le N$, $1 \le j \le N$, we have

$$\mathbf{u}_i^*(\omega)\mathbf{u}_j(\omega) = \mathbf{v}_i^*(\omega)\mathbf{v}_j(\omega) = \delta_{i,j}$$

with $\delta_{i,j}$ being the Kronecker delta. The SVD [20] of the array response matrix is

$$\widehat{\Pi}(\omega) = \sum_{j=1}^{N} \sigma_j(\omega)\mathbf{u}_j(\omega)\mathbf{v}_j^*(\omega). \tag{2.4}$$

The idea in using subspace migration is that the SVD provides a natural scale for the strength of the reflections reaching the array from different features of the target. Data filtering with subspace migration is an idea similar to apodization, where exoplanets or faint astronomical objects are imaged by obscuring the strong light from nearby stars with aperture control [39, 25]. The difference here is that the array is active, the data is in a broadband regime, and we exploit the coherence of the SVD over the different frequencies. Data filtering using the singular values of a matrix is also used as a regularization method in linear inverse problems [46].

Throughout this paper we make two simplifying assumptions regarding the migration functional (2.2). First, we assume that the pulses sent from each source are the same and independent of the frequency; i.e., $\widehat{f}(\vec{\mathbf{x}}_s, \omega) = 1$. The second assumption is that the multiplicative weights $d_j(\omega)$ used to define the filter D are binary; that is,

$$d_j(\omega) = \begin{cases} 1 & \text{if } j \in J(\omega), \\ 0 & \text{otherwise}, \end{cases} \tag{2.5}$$

for some set $J(\omega) \subset \{1, \ldots, N\}$ that determines which singular vectors of $\widehat{\Pi}(\omega)$ we keep. An optimization approach to select illuminations $\widehat{f}(\vec{\mathbf{x}}_s, \omega)$ and filter weights $d_j(\omega)$ in a way that enhances the quality of the images, as is done in [5], can also be carried out.

We focus attention on three subspace selection strategies.

1. The simplest strategy is to keep all singular vectors, so that all the data is migrated to obtain an image, without any selection. In this case $J^{\mathrm{KM}}(\omega) = \{1, \ldots, N\}$, so the filter D is the identity, and we recover the usual travel-time migration.

2. Another strategy is to keep for each frequency the strongest reflection, i.e., $J^{\mathrm{Detect.}}(\omega) = \{1\}$. This is good for detection and is very robust to noise. However, it is not good for imaging extended targets since the waves scattered by the edges are weaker than direct or specular reflections from the bulk of the target, and thus there is practically no information about the edges in the migrated data. This strategy is more closely related to the DORT (French acronym for decomposition of the time reversal operator) method [36], which is used for both imaging and physical time reversal, and which is designed to selectively image or focus energy on well-separated point-like targets. DORT in its basic form relies on the fact that the array response matrix for n such targets has rank n and that each singular vector corresponds to a different target [6]. In principle, migrating each singular vector separately forms an image of each single point-like target. When the point-like targets are not well separated and even when the surrounding medium is randomly inhomogeneous, an optimization approach introduced in [4] can determine weights $\{d_j(\omega)\}$ that image the targets one by one in a robust way.

3. Here we will remove the strongest reflections from an extended target so that we can focus on its edges. This is achieved by selecting singular vectors so that the normalized singular values $\sigma_j(\omega)/\sigma_1(\omega)$ of $\widehat{\Pi}(\omega)$ belong to some interval $[\alpha, \beta] \subset (0, 1)$; that is,

$$J^{\mathrm{SM}}(\omega; [\alpha, \beta]) = \left\{ j \mid \frac{\sigma_j(\omega)}{\sigma_1(\omega)} \in [\alpha, \beta] \right\}. \tag{2.6}$$

In this approach, we trade off some robustness to noise (detection capability) for the ability to focus selectively on the edges (imaging capability).

Using numerical simulations in the ultrasound regime, we compare next these approaches for imaging extended targets.

Remark 2.1. In simple situations it may be feasible to isolate the echoes coming from various parts of the reflectors by time-gating the data. However, for extended but far away reflectors this is difficult to do because the echoes arrive at almost the same time. The SVD-based subspace data filtering method proposed here is, in general, more computationally demanding than time-gating. But it has the advantage that it can be automated, thus avoiding any intervention. It is also robust with respect to additive noise for arrays with a large number of elements.

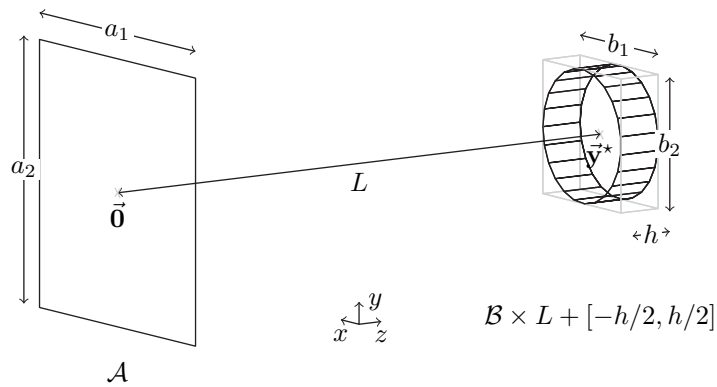

Figure 2. *Setup for array imaging.*

3. Numerical experiments. For simulations in the ultrasound regime we use the setup shown in Figure 2. The speed of propagation in the background medium (water) is $c_0 = 1.5\text{km/s}$, and the frequency band is [1.5MHz, 4.5MHz]. The central wavelength is $\lambda_0 = 0.5\text{mm}$, and the bandwidth $B = 3\text{MHz}$.

3.1. Setup for numerical simulations. We probe the medium with a square array in the xy plane with side (aperture) $a = 24.5\lambda_0$ and collocated sources and receivers in two different configurations. The first configuration has $N = 2500$ elements placed on a uniform 50×50 lattice. The second has $N = 100$ elements placed on a 10×10 uniform lattice.

The targets are thin prisms $\mathcal{B} \times L + [-h/2, h/2]$ with reflectivity $\rho(\vec{\mathbf{y}})$. We take first the case of constant reflectivity $\rho(\vec{\mathbf{y}}) = 1$. Then we consider in section 3.9 nonconstant reflectivities. The targets are at range $L = 100\lambda_0$. Their cross-range profile is $\mathcal{B} \subset [-b/2, b/2]^2$ with $b = 20\lambda_0$, and their thickness is $h = \lambda_0/5$. Off-centered targets are briefly examined in section 3.9. The targets are at first parallel to the array. In section 3.10 we also consider obliquely placed targets.

The synthetic data is generated using the Born approximation [8, section 13.1.2]

$$\widehat{\Pi}(\vec{\mathbf{x}}_r, \vec{\mathbf{x}}_s, \omega) \approx k^2 \int d\vec{\mathbf{y}} \rho(\vec{\mathbf{y}}) \widehat{G}_0(\vec{\mathbf{x}}_r, \vec{\mathbf{y}}, \omega) \widehat{G}_0(\vec{\mathbf{x}}_s, \vec{\mathbf{y}}, \omega), \tag{3.1}$$

where $\operatorname{supp} \rho = \mathcal{B} \times L + [-h/2, h/2]$. The integral in (3.1) is evaluated with the midpoint rule, which is equivalent to having a target with a lattice of point reflectors. In our computations we use $41 \times 41 \times 5$ points placed uniformly, at a distance no more than $\lambda_0/2$ apart.

We generated data for $N_{\text{freq}} = 51$ equally spaced frequencies ω_i in the bandwidth, which are 60KHz apart. This is enough for resolving numerically the coherent behavior of the singular values over the bandwidth. The frequency spacing we use corresponds roughly to a time window that is one-quarter of the travel time from the array to the target and back.

3.2. Multiple scattering. If we think of the target as a lattice of closely spaced point reflectors or "particles," then the Born approximation (3.1) takes into account only scattering paths involving a single particle. Our algorithm can of course be applied to any data, and, to see how multiple scattering influences the images that it produces, we also generated data

with second order multiple scattering ([8, section 13.1.4]), by modeling scattering paths that involve up to two particles:

$$\widehat{\Pi}(\mathbf{x}_r,\mathbf{x}_s,\omega) \approx k^2 \int d\vec{\mathbf{y}}\rho(\vec{\mathbf{y}})\widehat{G}_0(\vec{\mathbf{x}}_s,\vec{\mathbf{y}},\omega)\Big[\widehat{G}_0(\vec{\mathbf{x}}_r,\vec{\mathbf{y}},\omega) + k^2\int d\vec{\mathbf{y}}'\rho(\vec{\mathbf{y}}') \cdot \widehat{G}_0(\vec{\mathbf{x}}_r,\vec{\mathbf{y}}',\omega)\widehat{G}_0(\vec{\mathbf{y}},\vec{\mathbf{y}}',\omega)\Big]. \tag{3.2}$$

Here $\operatorname{supp}\rho = \mathcal{B}\times L + [-h/2,h/2]$.

We only considered a parallelepiped target with reflectivity $\rho = 1$, in the same configuration described in section 3.1. The target was discretized using $221\times 221\times 5$ points in order to get roughly 10 points per wavelength, although we went up to 21 points per wavelength ($413\times 413\times 11$ points) to validate our code. Since (3.2) involves convolutions, we can evaluate it efficiently using the FFT, as in a single step of the conjugate-gradient FFT or k-space Lippmann–Schwinger equation solvers (see, e.g., [23] for a review). Convergence is slow as the number of discretization points increases because we do not deal with the singularity at the diagonal of the kernel $\widehat{G}_0(\vec{\mathbf{y}},\vec{\mathbf{y}}',\omega)$.

For the 50×50 array and at the central frequency we found that the second order term in (3.2) represented roughly 51.6% of the power of the first order term (3.1); i.e., the ratio of their squared Frobenius norms was about 51.6%.

We generated subspace migration images using both first and second order scattering data, with the rescaled singular values in the interval $[0.001, 0.2]$ and with the 10×10 and the 50×50 arrays. We do not show here the images with the second order scattering data, because they are almost identical to the single scattering ones. This can be explained intuitively from (3.2), because in the second integral over $\vec{\mathbf{y}}'$ it is the volume of the penetrable target that plays the dominant role and not its edges (boundary). Our subspace migration approach looks for the edges of the target, and their effect on multiple scattering in the penetrable target is small. Multiple scattering should have a visible effect on the estimation of the actual value of the reflectivity inside the target and on the imaging of the support of impenetrable targets. We do not consider these problems here.

3.3. Singular values of the array response matrix. We compare in Figure 3 the singular values of the response matrix for both the 50×50 and the 10×10 arrays. To make the comparison more realistic we look at the array response matrix $\widehat{\Pi}(\omega)$ as an approximation of an $L^2(\mathcal{A})\to L^2(\mathcal{A})$ operator $\widehat{\Pi}_C(\omega)$ and plot the approximate singular values of $\widehat{\Pi}_C(\omega)$. That is, for g some function defined on $\mathcal{A}$ and $\mathbf{g} = [g(\mathbf{x}_1),\ldots,g(\mathbf{x}_N)]^T$ we have

$$\begin{aligned}(\Delta a)^2(\widehat{\Pi}(\omega)\mathbf{g})_r &= (\Delta a)^2\sum_{s=1}^{N}\widehat{\Pi}((\mathbf{x}_r,0),(\mathbf{x}_s,0),\omega)g(\mathbf{x}_s)\\ &\approx \int_{\mathcal{A}} d\mathbf{x}_s\widehat{\Pi}((\mathbf{x}_r,0),(\mathbf{x}_s,0),\omega)g(\mathbf{x}_s) = (\widehat{\Pi}_C(\omega)g)(\mathbf{x}_r),\end{aligned} \tag{3.3}$$

where $(\Delta a)^2 \equiv a^2/(\sqrt{N}-1)^2$ is the area associated, or covered, by an array sensor. The approximation above is a midpoint quadrature rule for the $L^2(\mathcal{A})$ inner product.

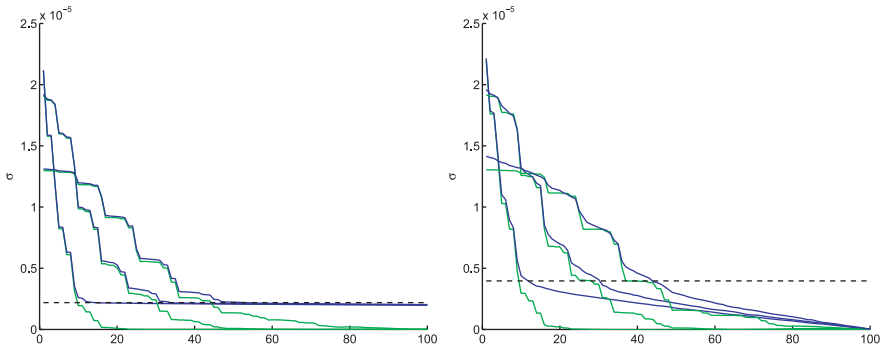

(a) SNR 0dB, 50×50 array (b) SNR 10dB, 10×10 array

Figure 3. *The first* 100 *singular values of the continuous array response matrix* $\widehat{\Pi}_C(\omega)$ *for noiseless (green line) and noisy (blue line) measurements for a rectangular target, and for frequencies* 1.5*MHz,* 3*MHz, and* 4.5*MHz. The dotted line is at the estimated largest singular value of the noise matrix.*

The spacing between elements in the 50×50 array is $\lambda_0/2$, so that it behaves as a continuum aperture (Nyquist criterion). As can be seen from Figure 3, the 10×10 array also behaves as an aperture, even though the spacing between elements is $2.5\lambda_0$. Indeed, the singular values for both arrays are similar when there is no noise.

Clearly there are only a few nonzero singular values, so $\widehat{\Pi}(\omega)$ is effectively a low-rank matrix (Figure 3). The first few right singular vectors correspond to the low-dimensional subspace of illuminations that produce echoes at the array.

The number of singular values that are effectively nonzero, that is, above some threshold relative to the largest singular value, increases with the frequency. This characteristic behavior has a theoretical explanation, at least in the Fraunhofer regime, as we show in section 4. In that section we also explain the staircase form of the singular values for square targets, which comes from separation of variables.

3.4. Singular values of the array response matrix with noise. To simulate instrument noise we added a noise matrix $W(\omega) \in \mathbb{C}^{N_r \times N_s}$ with zero mean uncorrelated Gaussian distributed entries having variance $\varepsilon p_{\text{avg}}$, that is, $W_{r,s}(\omega) \sim \mathcal{N}(0, \varepsilon p_{\text{avg}})$. Here $\varepsilon > 0$, and p_{avg} is the average power received per source, receiver, and frequency:

$$p_{\text{avg}} = \frac{1}{N_r N_s N_{\text{freq}}} \sum_{i=1}^{N_{\text{freq}}} \left\| \widehat{\Pi}(\omega_i) \right\|_F^2, \tag{3.4}$$

where $\|\cdot\|_F$ is the Frobenius matrix norm. The expected power of the noise $W(\omega_i)$ over all frequencies, receivers, and sources is

$$\mathbb{E}\left[\sum_{i=1}^{N_{\text{freq}}} \|W(\omega_i)\|_F^2 \right] = \varepsilon N_r N_s N_{\text{freq}} p_{\text{avg}}.$$

Since the total power of the signal received over all frequencies, receivers, and sources is $N_r N_s N_{\text{freq}} p_{\text{avg}}$, the SNR in dB is $-10 \log_{10} \varepsilon$.

The behavior with noise can be quantified relative to $\sigma_1[W(\omega)]$. To see this, let us return to the case $N = N_r = N_s$ (collocated sources and receivers) and use Corollary 8.6.2 in [20] which guarantees that for $1 \leq j \leq N$,

$$\left|\sigma_j\left[\widehat{\Pi}(\omega) + W(\omega)\right] - \sigma_j\left[\widehat{\Pi}(\omega)\right]\right| \leq \sigma_1\left[W(\omega)\right]. \tag{3.5}$$

Thus, the singular values of $\widehat{\Pi}(\omega)$ that are essentially zero become with noise singular values no larger than $\sigma_1[W(\omega)]$. This last quantity has been estimated asymptotically for large N by Geman [18] (see also [17]):

$$\sigma_1[W(\omega)] \approx 2\sqrt{\varepsilon N p_{\text{avg}}} \quad \text{for } N \text{ large.} \tag{3.6}$$

In Figure 3 we show the estimated effect of noise on the singular values of $\widehat{\Pi}_C(\omega)$ by a dotted line at $(\Delta a)^2 2\sqrt{\varepsilon N p_{\text{avg}}}$. This is a better estimate for the 50×50 array than for the 10×10 array, since (3.6) is an asymptotic result for large N.

The effect of noise is significantly higher when there are fewer receivers, which is what is expected. In fact, for the 10×10 array the noise influences more the singular values than for the 50×50 array, even if it is ten times weaker. The improvement in SNR with more elements in the array follows from

$$(\Delta a)^2 \sigma_1[W(\omega)] \approx (\Delta a)^2 2\sqrt{\varepsilon N p_{\text{avg}}} = \frac{2a^2\sqrt{\varepsilon N p_{\text{avg}}}}{(\sqrt{N}-1)^2} = \mathcal{O}(N^{-1/2}) \quad \text{for } N \text{ large.} \tag{3.7}$$

The bound (3.5) is rather conservative for the largest singular values, as can be seen with a simple example. Assuming $\widehat{\Pi}(\omega)$ has rank $r < N$, its SVD can be rewritten as

$$\widehat{\Pi}(\omega) = \begin{bmatrix} U_1 & U_2 \end{bmatrix} \begin{bmatrix} \Sigma & \\ & 0 \end{bmatrix} \begin{bmatrix} V_1^* \\ V_2^* \end{bmatrix},$$

where $[U_1, U_2]$ and $[V_1, V_2]$ are unitary matrices and $\Sigma = \text{diag}(\sigma_1[\widehat{\Pi}(\omega)], \ldots, \sigma_r[\widehat{\Pi}(\omega)])$. Now if the vectors in the span of U_1 and V_1 are not noisy, then we can think of $\text{Range}\, W(\omega) \subset \text{Range}\, U_2$ and $\text{Range}\, W^*(\omega) \subset \text{Range}\, V_2$. Let us further assume that we do have $W(\omega) = U_2 U_2^* W(\omega) V_2 V_2^*$ and that the SVD of $U_2^* W(\omega) V_2$ is $U_W \Sigma_W V_W^*$ with $\sigma_1[\Sigma_W] \leq \sigma_r[\Sigma]$. Then the SVD of the noisy measurements has the form

$$\widehat{\Pi}(\omega) + W(\omega) = \begin{bmatrix} U_1 & U_2 U_W \end{bmatrix} \begin{bmatrix} \Sigma & \\ & \Sigma_W \end{bmatrix} \begin{bmatrix} V_1^* \\ V_W^* V_2^* \end{bmatrix}.$$

Thus, at least in this very simple case, the largest singular values of $\widehat{\Pi}(\omega) + W(\omega)$ remain those of $\widehat{\Pi}(\omega)$.

3.5. Image display conventions. Most of the images we show in section 3 are obtained with the search point $\vec{\mathbf{y}}^S$ in a domain $\mathcal{D}$ consisting of three slices $z = L$, $x = 0$, and $y = 0$ passing through the center $\vec{\mathbf{y}}^\star = (\mathbf{0}, L)$ of the target. Each slice is discretized with 40×40 points. The cross-range dimension of the slices is $30\lambda_0$, and the dimension in range is $10\lambda_0$.

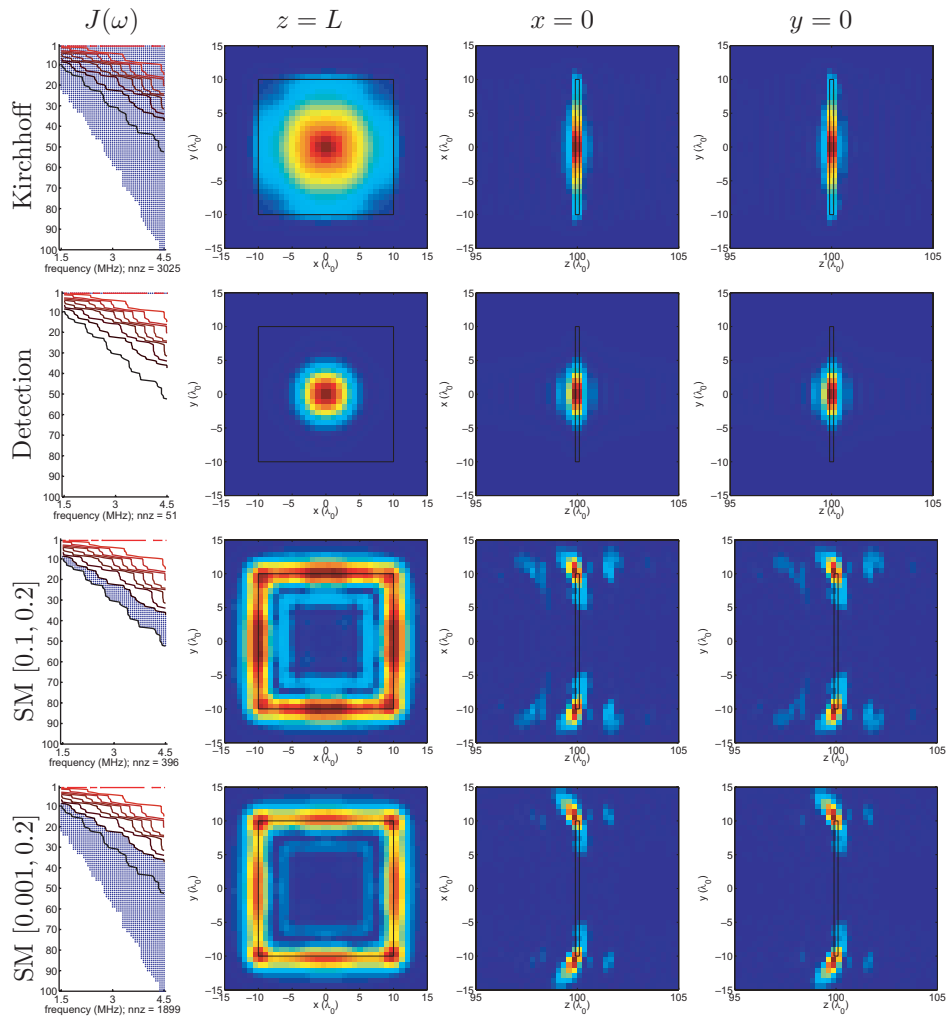

Figure 4. *Comparison of different methods for imaging a rectangular target with data captured on a* 50×50 *array and with infinite SNR.*

We plot $\left|\mathcal{I}(\vec{\mathbf{y}}^S)\right| / \max_{\vec{\mathbf{y}}^S \in \mathcal{D}}(\left|\mathcal{I}(\vec{\mathbf{y}}^S)\right|)$, and we used the same scale for each row of plots. For reference, the outline of the target is superposed in black.

We show the sets $J(\omega_i)$ that define the class of filtering operators that we consider as blue dots on a contour plot of the rescaled singular values $\sigma_j(\omega_i)/\sigma_1(\omega_i)$, with the frequency ω_i as the abscissa and the singular value index j as the ordinate. The contours are spaced every 10%. When there is noise in the data we add a thick green line. The singular values above this line are above the expected noise level $2(\Delta a)^2\sqrt{\varepsilon p_{\text{avg}} N}$ (see section 3.4).

3.6. Selected subspace migration imaging. We compare in Figures 4 and 5 the images obtained with the different filtering strategies described in section 2.2, for the 50×50 array with and without noise. To emphasize the fact that the array response matrix $\widehat{\Pi}(\omega)$ is low rank, instead of taking all the singular values for travel-time migration, we take at a given

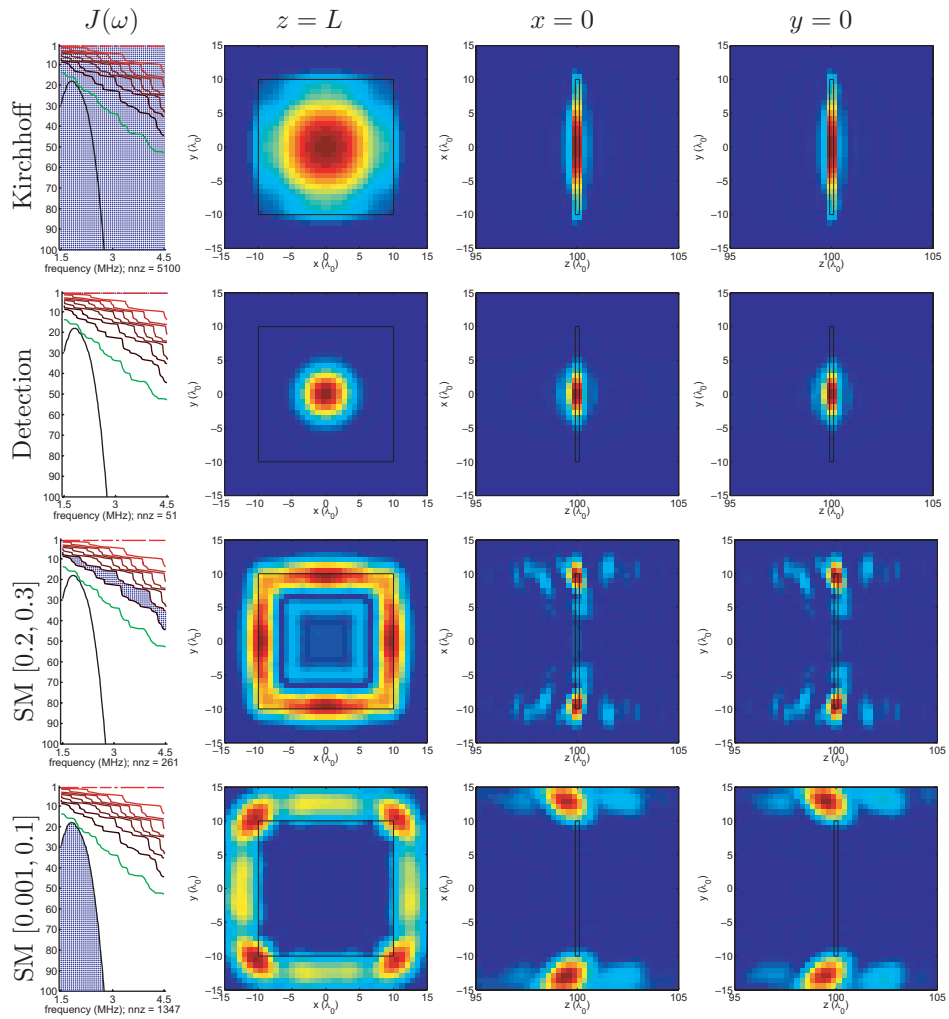

Figure 5. *Comparison of different methods for imaging a rectangular target with data captured on a* 50×50 *array and with* $0dB$ *SNR.*

frequency ω_i only the singular values larger than 0.1% of $\sigma_1[\widehat{\Pi}(\omega_i)]$.

Travel-time migration works well in recovering the object as a whole. In detection, only the largest singular value is used, so the image shows the strongest reflection which comes from the center of the object. This is good for detecting targets but not for imaging extended targets because information about the edges is lost.

Keeping intermediate singular values, say between 10% and 20% of the largest singular value, gives images that show the edges of the object. It appears from our experiments that taking all the singular values below some threshold (say 20%) improves the images in range. This is probably because information about the perimeter of the object is present redundantly in the intermediate singular values (see section 4).

We make two general observations regarding the contour plots for the singular values (Figures 4 and 5). First, the number of singular values that are within 10% of the largest one increases with frequency. Second, the noise influences the higher frequencies more. In fact

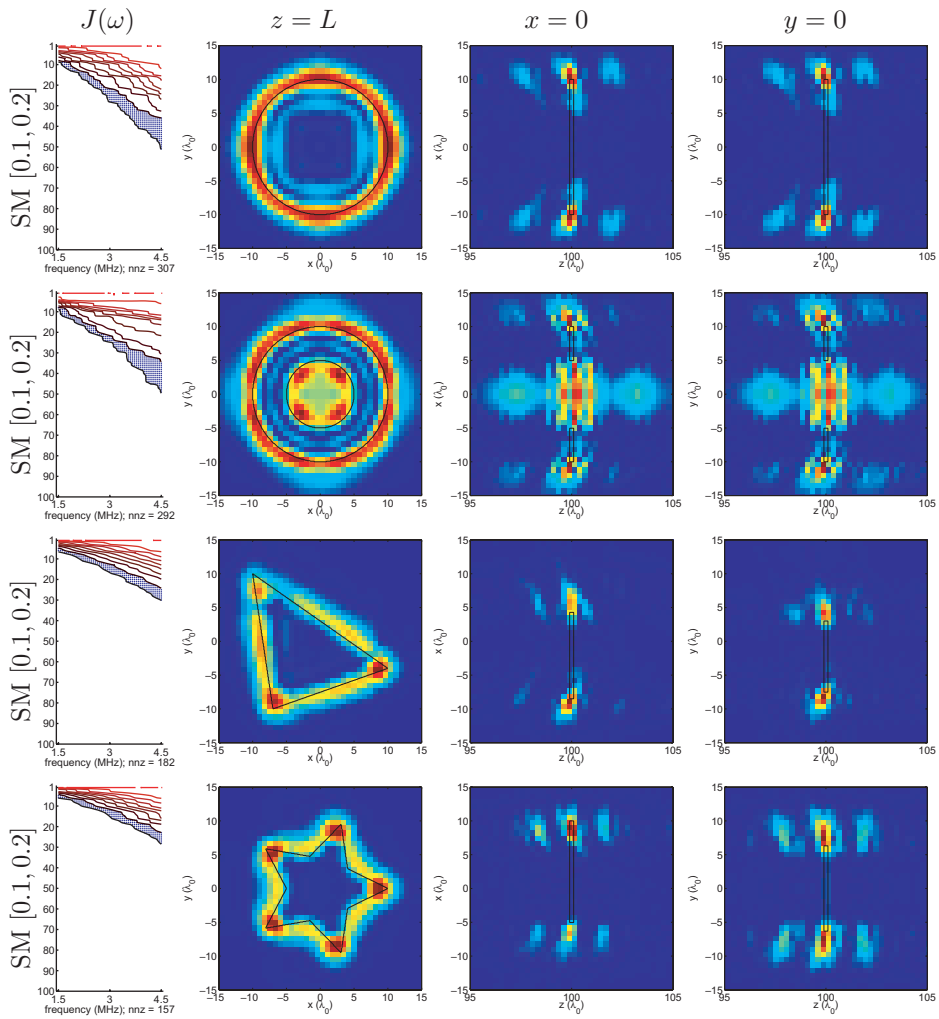

Figure 6. *Edge illumination of other targets, with infinite SNR.*

for the data with 0dB SNR there are no singular values below the 10% contour for the upper half of the bandwidth (the "dome" in Figure 5). This separation does not occur with fewer receivers (Figure 8).

In Figure 6 we use the edge illumination algorithm for targets that have different cross-range profiles. The results are similar to those for the rectangular target, so we show only images with rescaled singular values between 10% and 20%. Note that the images peak close to the corners because scattering is stronger there.

3.7. Influence of array size on imaging with noisy data. Travel-time migration and detection with the top singular value are very stable in the presence of noise: the images with 0dB SNR are very similar to the images with infinite SNR data. The edge illumination method is naturally more sensitive to noise, but if we take singular values above the noise level, the results are similar. If we go below the noise level, we still get images of the edges,

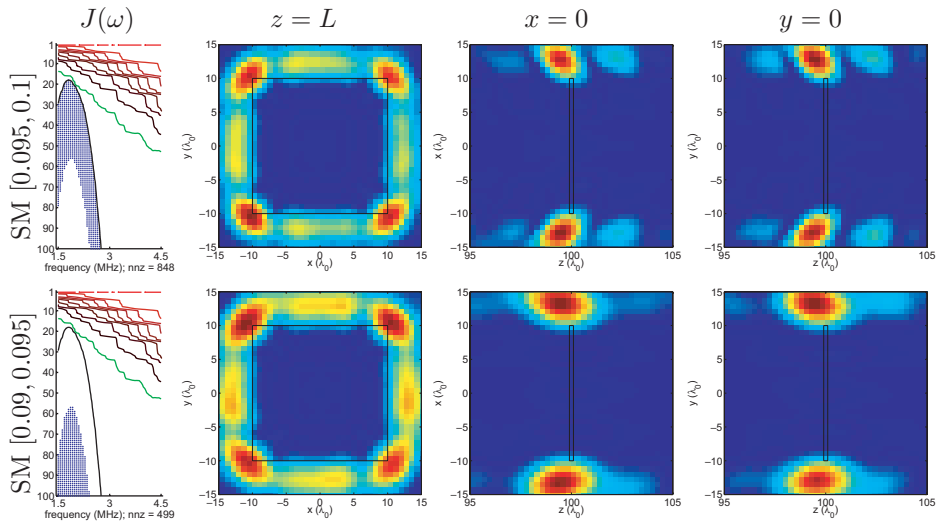

Figure 7. *Imaging with the bottom* 10% *of the rescaled singular values and with* 0*dB SNR data, captured with a* 50×50 *array gives blurry images. This robust-to-noise behavior should be compared to that of an array with fewer sensors and the same aperture (Figure* 8*).*

but they appear blurred in both range and cross-range. This is shown in Figures 7 and 8.

For the 50×50 array, edge illumination imaging is robust to noise: blurry images can be obtained even with singular values that are 10% below the largest one (Figure 7). This is because of the large number of elements in the array (section 3.4) and because we use only the first 100 singular vectors.

With fewer array elements the images break down more easily. For the 10×10 array, imaging with the bottom 5% of the rescaled singular values (Figure 8) gives unacceptable images. The breakdown happens mostly outside the target, where there is no information since there are no echoes.

3.8. Sparse sensor arrays. We show in Figure 9 images obtained with progressively sparser sensor placement in the arrays and with infinite SNR. Here by sparse we mean that the array has fewer sensors but the same overall dimensions. The possibility of being able to use sparse arrays is important because arrays with many sensors can be expensive. Of course, the sensors must not be too far apart because then they will not behave like an array at all. It simplifies the theory when we treat $\widehat{\Pi}(\omega)$ as the $L^2(\mathcal{A}) \to L^2(\mathcal{A})$ operator $\widehat{\Pi}_C(\omega)$, and in the numerics it avoids aliasing. The rule of thumb (motivated by the Nyquist criterion) is to have array elements that are no more than $\lambda_0/2$ apart. This is why in most of our numerical simulations we use a large array with 50×50 elements.

In the numerical experiments we see that it is possible to obtain comparable images even with a small 8×8 array, where its elements are 7 times farther apart than in the 50×50 array. The images obtained with travel-time migration and detection using the top singular value behaved similarly, so we do not show them.

Having a small number of sensors in the array is not a good idea because imaging is much more sensitive to noise. As we saw in section 3.4, the effect of noise decreases with the number

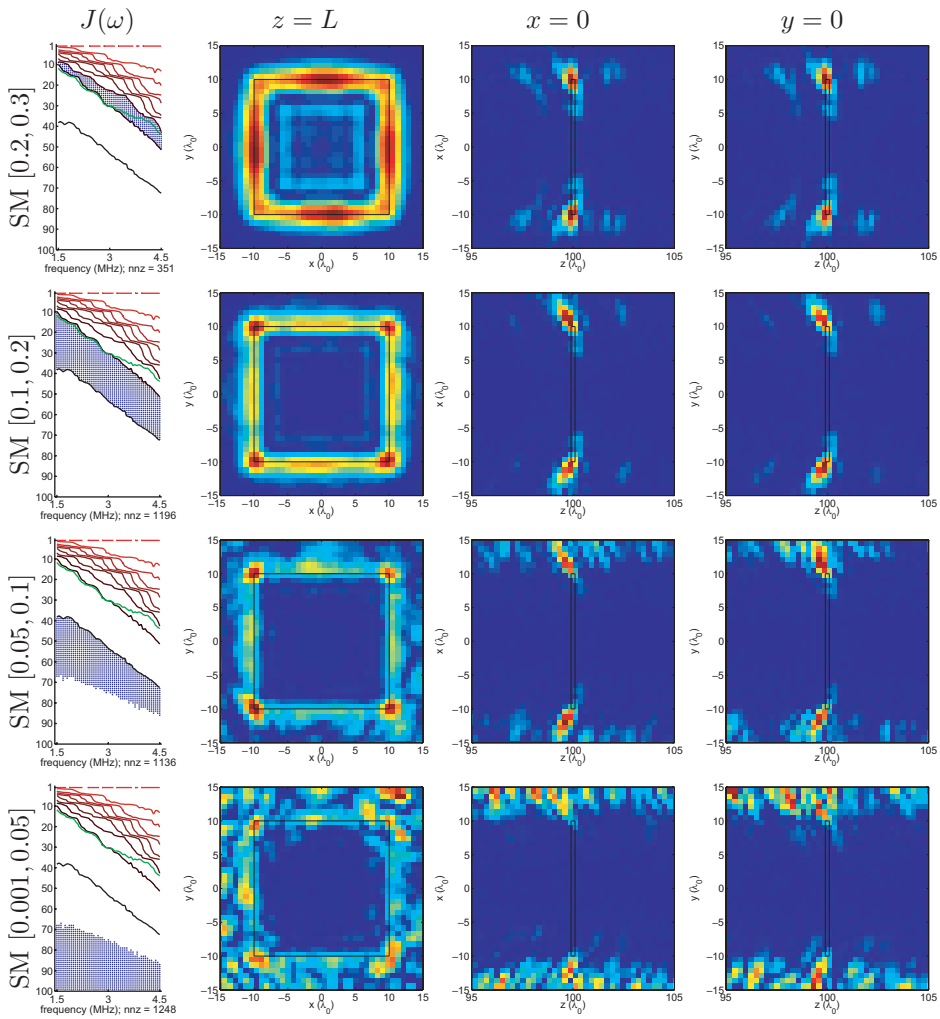

Figure 8. *Images obtained with the bottom* 30% *of the rescaled singular values and with* 10*dB data, captured with a* 10×10 *array. When we use the bottom* 5% *of rescaled singular values the images break down. This should be contrasted with the robustness of the images for the* 50×50 *array in Figure* 7.

of array elements. With infinite SNR, good images can be obtained as long as the number of array elements is larger than the effective rank $N^\star(\omega)$ of the operator $\widehat{\Pi}_C(\omega)$, at the highest frequency in the bandwidth.

3.9. Off-centered targets and nonconstant reflectivities. We see from Figure 10 that subspace migration is unaffected by shifts of the reflector in the xy plane. We computed subspace migration images for a parallelepiped target with dimensions $10\lambda_0 \times 10\lambda_0 \times \lambda_0/5$, centered at the point $(5\lambda_0, 5\lambda_0, 100\lambda_0)$. The images are centered at the point $(0, 0, 100\lambda_0)$, following the conventions outlined in section 3.5.

We also tested how subspace migration behaves when the reflectivity is not constant, using two configurations. In the first, the target is a parallelepiped with dimensions $b \times b \times h$ (as

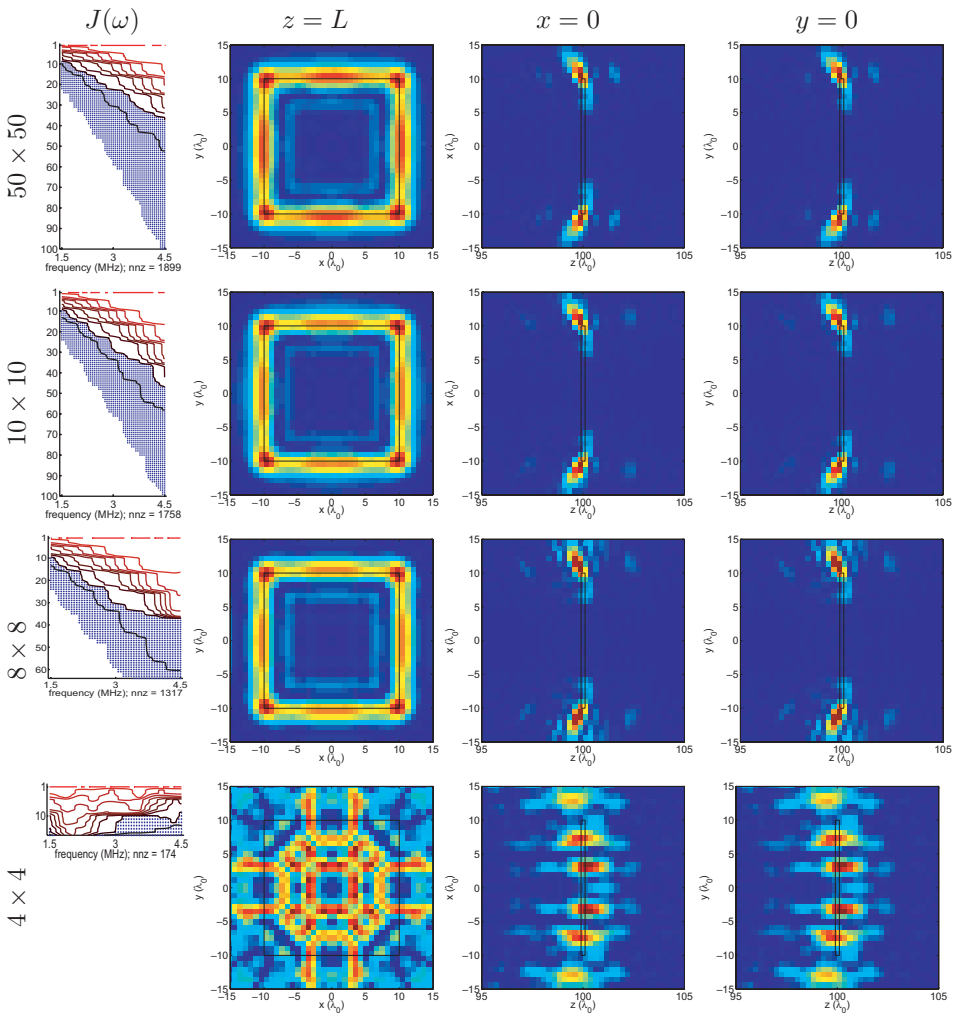

Figure 9. *Using arrays with identical aperture but fewer sensors, and with infinite SNR. The distances between sensors are from top to bottom:* $0.5\lambda_0$, $2.72\lambda_0$, $3.5\lambda_0$, *and* $8.16\lambda_0$. *The rescaled singular values are in the interval* $[0.001, 0.2]$. *The plots are shorter for sparser arrays because there are fewer singular values.*

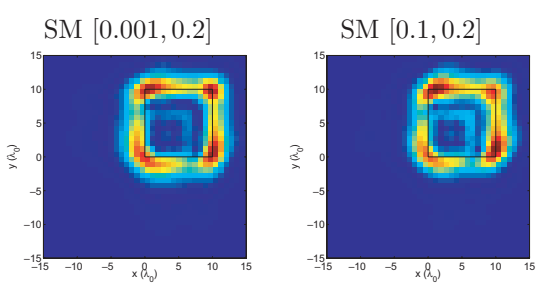

Figure 10. *Edge illumination of an off-center rectangular target.*

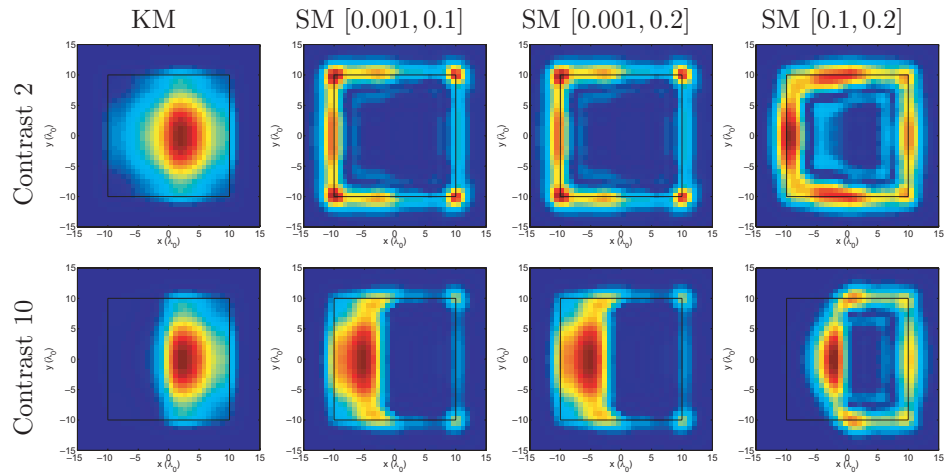

Figure 11. *Subspace migration images in the xy plane of a rectangular target made with two reflectivities. The higher reflectivity is in $x > 0$. Two different contrasts (ratio of highest to lowest reflectivity) are considered.*

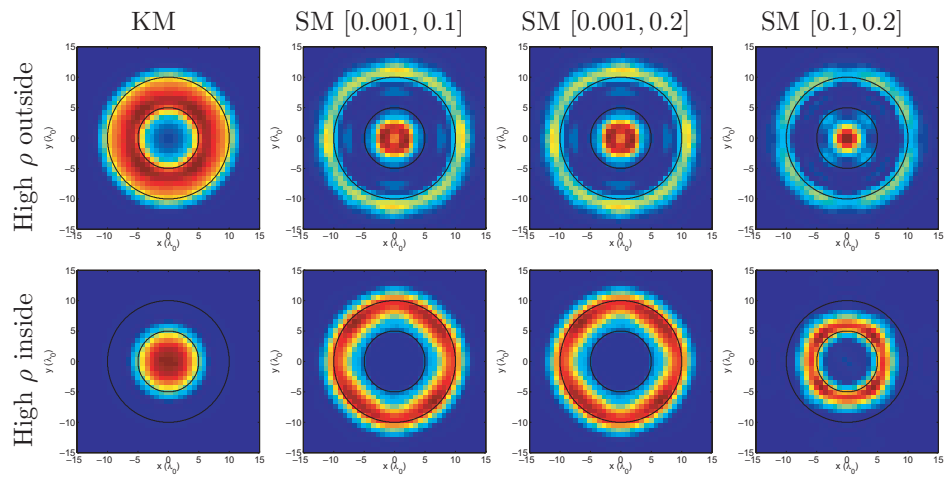

Figure 12. *Subspace migration images in the xy plane of a circular target with two reflectivities with contrast (ratio of highest to lowest reflectivity) of* 10. *First row: the higher reflectivity is on the outside. Second row: the higher reflectivity is on the inside.*

in section 3.1), where the reflectivity is different depending on the sign of x. In the second configuration (Figure 12) the target is a cylinder of diameter b and depth h, having a different reflectivity in the concentric cylinder of diameter $b/2$. We show images when the higher reflectivity is either on the inside ($|\boldsymbol{\xi}| < b/2$) or on the outside ($b/2 \leq |\boldsymbol{\xi}| \leq b$).

In Figure 11 we also see the effect of the contrast (ratio of highest to lowest reflectivity) on the images. For low contrast, subspace migration images are comparable to those for a constant reflectivity where the edges are emphasized when we remove the largest singular values. However, the edges for the higher reflectivities appear sharper than those for the lower reflectivities. With higher contrast, in both Figures 11 and 12, we see that when we take all

the singular values below a threshold we mask the stronger reflections, which come from the highest reflectivity region of the target, and thus enhance the part of the reflector that is not well imaged with the plain travel-time migration.

For nonconstant reflectivities, therefore, imaging with subspace filtering does not detect edges but removes the stronger components of the usual travel-time migration to reveal the faintest ones. If we can use low enough singular values, it may be possible to image the edges of the low reflectivity region. A deeper study of the information contained in the singular subspaces of the response matrix for nonconstant reflectivities is left for future studies.

3.10. Oblique targets. In Figure 13 we consider travel-time migration, detection with the top singular value, and our edge illumination approach when the target is not parallel to the array. The rectangular target we considered has the same dimensions $20\lambda_0 \times 20\lambda_0 \times \lambda_0/5$ as before, but it is rotated by $\pi/12$ around the x axis or around the $x = y, z = L$ axis. The image domain is a box with dimensions $[-15\lambda_0, 15\lambda_0]^2 \times [-5\lambda_0, 5\lambda_0]$, with the same center $\vec{\mathbf{y}}^\star$ as the target. It is discretized with 40^3 points.

From the images with travel-time migration and detection with the top singular value images we see that the edges parallel to and close to the array are the ones that produce the strongest reflections. In fact, detection with the top singular value focuses only on the closest feature, edge or corner, to the array. Because of the orientation, the interior of the target and the other edges do not appear in the images: the echoes from the waves hitting these features do not reach the array and are overpowered by the specular reflections.

The edge illumination approach obscures these strong reflections and reveals features coming from edges or corners that could not be seen in the travel-time migration image. For both targets we can see corners as stronger features. The edges that are prominent in the travel-time migration images are masked.

4. Analysis in the Fraunhofer regime. We now show that the qualitative behavior of the singular values of the array response matrix can be explained in the regime of Fraunhofer diffraction by using some results for space and wavenumber limiting operators.[1] The analysis also explains why choosing intermediate singular values images well the edges of the target.

4.1. The Fraunhofer regime. With the characteristic length scales of the imaging problem we define the following dimensionless parameters:

$$\theta_a = \frac{k_0 a^2}{L}, \quad \theta_b = \frac{k_0 b^2}{L}, \quad \theta_h = \frac{k_0 h^2}{L}, \quad \text{and} \quad \theta_{ab} = \frac{k_0 ab}{L}.$$

Here $k_0 = \omega_0/c_0 = 2\pi/\lambda_0$ is the central wavenumber, λ_0 is the central wavelength, a is the array aperture, L is the range, b is the diameter of the target, and h is its thickness (see Figure 2).

The parameter θ_a is the Fresnel number of the array. By analogy we also call the other three parameters Fresnel numbers (as in [5]). The scaling regime we consider is a particular

[1]Space and wavenumber limiting operators are discussed in more detail in section 4.5. They are also called "space and frequency limiting" [38] or "time and band limiting" operators [40], depending on the interpretation of the Fourier space. To avoid confusion with the frequency ω, we use here "wavenumber" instead of "spatial frequency."

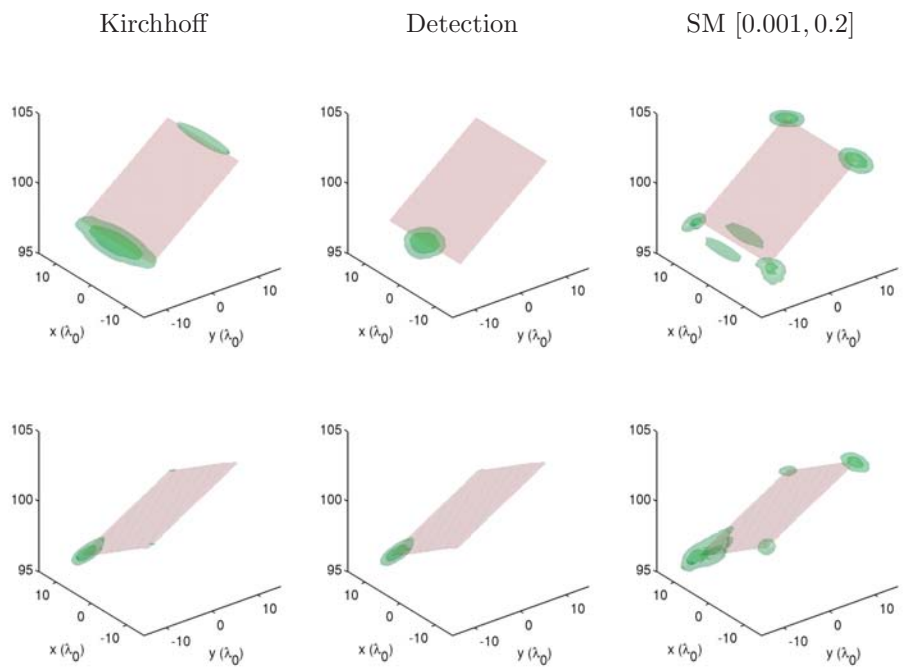

Figure 13. *Images for a rectangular target rotated by $\pi/12$ around the x axis (top row) or the $x = y, z = L$ axis (bottom row), with infinite SNR data. The true target appears in pink. Only the isosurfaces $1/4$ and $1/2$ of the image are plotted.*

case of the usual Fraunhofer diffraction regime [8, section 8.3], in which the focal spot size is small relative to the array aperture; that is,

$$\frac{\lambda_0 L}{a} \ll a \Leftrightarrow \theta_a \gg 1. \tag{4.1}$$

We also require that the range is large so that

$$\frac{a^2}{L^2} \ll \frac{1}{\theta_a} \ll 1 \tag{4.2}$$

and that the target is small with respect to the aperture; that is, $b \ll a$ and $\theta_b \ll 1$. We assume that the target contains at least a few focal spot sizes; that is,

$$b \geq \frac{\lambda_0 L}{a} \Leftrightarrow \theta_{ab} \geq 1. \tag{4.3}$$

We work with thin reflectors satisfying $\theta_h \ll 1$ and $h \ll a \ll L$. Moreover, we assume that the thickness of the reflector h is small compared to $L^2/(k_0 a^2)$, the range resolution of single frequency images [8, Chapter 8.8]:

$$h \ll \frac{L^2}{k_0 a^2} \Leftrightarrow \frac{h\theta_a}{L} \ll 1. \tag{4.4}$$

4.2. Ultrasonic and optical imaging. The setup for the numerical simulations of section 3 is for high frequency ultrasonic imaging which, however, does not fall into the Fraunhofer scaling regime as we defined it in section 4.1. Indeed, we take the frequency band $[1.5\text{MHz}, 4.5\text{MHz}]$ so that, for the sound speed $c_0 = 1.5\text{km/s}$ in water, we get a central wavelength $\lambda_0 = 0.5\text{mm}$. The range is $L = 100\lambda_0 = 5\text{cm}$, and the array aperture $a = 24.5\lambda_0 = 1.225\text{cm}$ is comparable to the linear size of the reflector $b = 20\lambda_0 = 1\text{cm}$. The Fresnel numbers in our simulations are

$$\theta_a \approx 12\pi, \quad \theta_b = 8\pi, \quad \theta_h = \frac{1}{1250}\pi, \quad \text{and} \quad \theta_{ab} = \frac{49}{5}\pi,$$

so we are clearly not in the Fraunhofer regime of section 4.1.

The Fraunhofer regime arises naturally in optical imaging, where the typical wavelength is $\lambda_0 = 0.5\mu\text{m}$ and where, for example, the range may be taken to be $L = 3\text{m}$, the array aperture $a = 2\text{cm}$, and the reflector size $b = 0.1\text{mm}$. This gives

$$1 \ll \theta_a \approx 1.68 \times 10^3 \ll \frac{L^2}{a^2} = 2.25 \times 10^4$$

and

$$\theta_{ab} \approx 8.38 \gg \theta_b \approx 0.042,$$

so it corresponds roughly to the assumptions in section 4.1.

Numerical simulations in the Fraunhofer regime are very demanding computationally because the array aperture contains about 10^4 central wavelengths in each direction. Since the sensors in the array should be separated by at most a λ_0 distance, we need about 10^8 sensors. This is why we do not carry out numerical simulations in the Fraunhofer regime.

In the ultrasonic regime of our numerical setup, an extended Fraunhofer regime with $\theta_b \sim \theta_{ab} \sim 1$ is more appropriate. The results of the numerical simulations indicate, however, that the qualitative behavior of our imaging algorithm is nearly as predicted by the Fraunhofer theory. We discuss briefly in section 5 the extended Fraunhofer regime and show how it captures better the behavior of the singular values of the array response matrix in the numerical simulations.

4.3. The array response matrix in the Fraunhofer regime. Three key approximations are made in the Fraunhofer regime. The first is the Born approximation [8, section 13.1.2], and the second is the paraxial approximation $\widehat{G}_0(\vec{\mathbf{x}}, \vec{\mathbf{y}}, \omega) \approx \widehat{\mathcal{G}}_0(\vec{\mathbf{x}}, \vec{\mathbf{y}}, \omega)$, which simplifies with the scalings of the Fraunhofer regime as described below. With the two first approximations we may write

$$\widehat{\Pi}(\vec{\mathbf{x}}_r, \vec{\mathbf{x}}_s, \omega) \approx \widehat{\Pi}_F(\vec{\mathbf{x}}_r, \vec{\mathbf{x}}_s, \omega) = k^2 \int_{\mathcal{B}\times L+[-h/2,h/2]} d\vec{\mathbf{y}}\rho(\vec{\mathbf{y}})\widehat{\mathcal{G}}_0(\vec{\mathbf{x}}_r, \vec{\mathbf{y}}, \omega)\widehat{\mathcal{G}}_0(\vec{\mathbf{x}}_s, \vec{\mathbf{y}}, \omega), \tag{4.5}$$

where $\rho(\vec{\mathbf{y}})$ is the reflectivity of the target. The third and last is the "continuum" approximation of the $L^2(\mathcal{A})$ inner product by $(\Delta a)^2 \equiv a^2/(\sqrt{N}-1)^2$ times the $\mathbb{C}^N$ inner product. Instead of studying the matrix $[\widehat{\Pi}_F(\vec{\mathbf{x}}_r, \vec{\mathbf{x}}_s, \omega)]_{r,s=1}^N$, we study the operator $\widehat{\Pi}_F(\omega) : L^2(\mathcal{A}) \to L^2(\mathcal{A})$ defined by

$$(\widehat{\Pi}_F(\omega)f)(\mathbf{x}) = \int_{\mathcal{A}} d\mathbf{y} f(\mathbf{y})\widehat{\Pi}_F((\mathbf{x}, 0), (\mathbf{y}, 0), \omega). \tag{4.6}$$

We now describe how to obtain the paraxial approximation to the free space Green's function

$$\widehat{G}_0(\vec{\mathbf{x}},\vec{\mathbf{y}},\omega) \approx \widehat{\mathcal{G}}_0(\vec{\mathbf{x}},\vec{\mathbf{y}},\omega) = \frac{1}{4\pi L}\exp\left[ik\left(L+\eta+\frac{|\mathbf{x}|^2}{2L}-\frac{\mathbf{x}\cdot\boldsymbol{\xi}}{L}\right)\right], \tag{4.7}$$

for $\vec{\mathbf{x}} = (\mathbf{x},0) \in \mathcal{A}$ and $\vec{\mathbf{y}} = (\boldsymbol{\xi}, L+\eta) \in \mathcal{B}\times L+[-h/2,h/2]$. The first step is to notice that for $\vec{\mathbf{x}}$ in the array and $\vec{\mathbf{y}}$ in the target, the denominator in the free space Green's function (1.2) is approximately $4\pi L$ since

$$|\vec{\mathbf{x}}-\vec{\mathbf{y}}| = \left[(L+\eta)^2+|\mathbf{x}-\boldsymbol{\xi}|^2\right]^{\frac{1}{2}} = L\left[1+\mathcal{O}\left(\frac{h}{L}\right)+\mathcal{O}\left(\frac{a^2}{L^2}\right)\right] \approx L. \tag{4.8}$$

The approximation of the phase in the Green's function (1.2) comes from

$$\begin{aligned} k\,|\vec{\mathbf{x}}-\vec{\mathbf{y}}| &= k\left(L+\eta+\frac{|\mathbf{x}|^2}{2L}-\frac{\mathbf{x}\cdot\boldsymbol{\xi}}{L}\right)+\mathcal{O}\left(\theta_b+\theta_h+\theta_a\frac{h}{L}+\theta_a\frac{a^2}{L^2}\right)\\ &\approx k\left(L+\eta+\frac{|\mathbf{x}|^2}{2L}-\frac{\mathbf{x}\cdot\boldsymbol{\xi}}{L}\right). \end{aligned} \tag{4.9}$$

In both (4.8) and (4.9), we can neglect the terms in $\mathcal{O}(\cdot)$ because of the assumptions made in the Fraunhofer regime (section 4.1).

Next we characterize the Fraunhofer regime array response matrix $\widehat{\Pi}_F(\omega)$ in terms of a known class of linear operators.

4.4. The singular value decomposition of the array response matrix. For reflectivities of the form $\rho(\vec{\mathbf{y}}) = \chi_{\mathcal{B}}(\boldsymbol{\xi})\rho_L(\eta)$, where $\vec{\mathbf{y}} = (\boldsymbol{\xi}, L+\eta)$ is in the target, we relate $\widehat{\Pi}_F(\vec{\mathbf{x}}_r,\vec{\mathbf{x}}_s,\omega)$ to a space and wavenumber limiting operator. We have the following.

Proposition 4.1. *When the array is invariant under reflections about the origin ($-\mathbf{x}\in\mathcal{A} \Leftrightarrow \mathbf{x}\in\mathcal{A}$), then*

$$\widehat{\Pi}_F(\omega) = \frac{\widehat{\rho}_L(-2k)}{4}\mathcal{U}(\omega)\mathcal{R}\mathcal{A}Q_{\frac{k}{L}\mathcal{B}}\mathcal{A}\mathcal{U}(\omega).$$

Here $\mathcal{U}(\omega)$ is the unitary operator

$$(\mathcal{U}(\omega)f)(\mathbf{x}) = (4\pi L)\widehat{\mathcal{G}}_0(\vec{\mathbf{x}},\vec{\mathbf{y}}^\star,\omega)f(\mathbf{x}) = \exp\left[ik\left(L+\frac{|\mathbf{x}|^2}{2L}\right)\right]f(\mathbf{x}),$$

which is multiplication by a phase, and with $\vec{\mathbf{x}} = (\mathbf{x},0)$ and $\vec{\mathbf{y}}^\star = (\mathbf{0},L)$. The operator $\mathcal{A}: L^2(\mathbb{R}^2)\to L^2(\mathbb{R}^2)$ is the orthogonal projection onto the set of functions supported on $\mathcal{A}$,

$$(\mathcal{A}f)(\mathbf{x}) = \chi_{\mathcal{A}}(\mathbf{x})f(\mathbf{x}),$$

and the operator $Q_{\frac{k}{L}\mathcal{B}}: L^2(\mathbb{R}^2)\to L^2(\mathbb{R}^2)$ projects orthogonally onto the set of functions that have a Fourier transform supported on the set $\frac{k}{L}\mathcal{B} \equiv \left\{\mathbf{x}\in\mathbb{R}^2 \mid \frac{L}{k}\mathbf{x}\in\mathcal{B}\right\}$,

$$Q_{\frac{k}{L}\mathcal{B}} = \mathcal{F}^{-1}\left(\frac{k}{L}\mathcal{B}\right)\mathcal{F},$$

where $\mathcal{F}$ is the Fourier transform. Finally, $\mathcal{R}$ is reflection about the origin $(\mathcal{R}f)(\mathbf{x}) \equiv f(-\mathbf{x})$.

The factorization of the operator $\widehat{\Pi}_F(\omega)$ in Proposition 4.1 has a simple physical interpretation. Since $\mathcal{U}(\omega)$, $\mathcal{A}$, and $\mathcal{R}$ commute, the operator $\widehat{\Pi}_F(\omega)$ is a multiple of $\mathcal{A}\mathcal{U}(\omega)\mathcal{R}Q_{\frac{k}{L}\mathcal{B}}\mathcal{U}(\omega)\mathcal{A}$, whose action from right to left means that the illumination is first restricted to the array, it is then propagated to the reflector by $\mathcal{U}(\omega)$, it scatters off the reflector according to $Q_{\frac{k}{L}\mathcal{B}}$ (in the Fraunhofer regime), it is reflected about the origin, then propagated back to the array, and, finally, restricted to the array again.

The operator $\mathcal{A}Q_{\frac{k}{L}\mathcal{B}}\mathcal{A}$ of Proposition 4.1 is a space and wavenumber (or time and frequency) limiting operator, a product of orthogonal projections, encountered in the study of functions that are well localized as are their Fourier transforms. The connection between the Fraunhofer response matrix and such operators, in the context of imaging a slit with a linear array in two dimensions, is considered in [5].

We review the properties of time and frequency limiting operators in section 4.5. In particular, $\mathcal{A}Q_{\frac{k}{L}\mathcal{B}}\mathcal{A}$ is Hilbert–Schmidt, is self-adjoint, and has a discrete real spectrum with positive eigenvalues. So the SVD of $\widehat{\Pi}_F(\omega)$ follows by Proposition 4.1 from the spectral decomposition of $\mathcal{A}Q_{\frac{k}{L}\mathcal{B}}\mathcal{A}$.

Proposition 4.2. *The singular values of $\widehat{\Pi}_F(\omega)$ are for $n \in \mathbb{N}$*

$$\sigma_n[\widehat{\Pi}_F(\omega)] = \frac{|\widehat{\rho}_L(-2k)|}{4}\sigma_n[\mathcal{A}Q_{\frac{k}{L}\mathcal{B}}\mathcal{A}],$$

with associated right and left singular functions

$$\begin{aligned} v_n[\widehat{\Pi}_F(\omega)] &= \mathcal{U}^*(\omega)v_n[\mathcal{A}Q_{\frac{k}{L}\mathcal{B}}\mathcal{A}] \quad \textit{and} \\ u_n[\widehat{\Pi}_F(\omega)] &= \arg(\widehat{\rho}_L(-2k))\mathcal{U}(\omega)\mathcal{R}v_n[\mathcal{A}Q_{\frac{k}{L}\mathcal{B}}\mathcal{A}], \end{aligned}$$

where $\arg(\cdot)$ *denotes the complex argument.*

Proof of Proposition 4.1. Applying $\mathcal{U}^*(\omega)\widehat{\Pi}_F(\omega)\mathcal{U}^*(\omega)$ to a function f gives

$$\begin{aligned} &(\mathcal{U}^*(\omega)\widehat{\Pi}_F(\omega)\mathcal{U}^*(\omega)f)(\mathbf{x}_r) \\ &\qquad = (4\pi L)^2 \int_{\mathcal{A}} d\mathbf{x}_s f(\mathbf{x}_s)\overline{\widehat{\mathcal{G}}_0(\vec{\mathbf{x}}_r, \vec{\mathbf{y}}^\star, \omega)}\widehat{\Pi}_F(\vec{\mathbf{x}}_r, \vec{\mathbf{x}}_s, \omega)\overline{\widehat{\mathcal{G}}_0(\vec{\mathbf{x}}_s, \vec{\mathbf{y}}^\star, \omega)}, \end{aligned}$$

where $\vec{\mathbf{y}}^\star = (\mathbf{0}, L)$, $\vec{\mathbf{x}}_s = (\mathbf{x}_s, 0)$, and $\vec{\mathbf{x}}_r = (\mathbf{x}_r, 0)$. With (4.5) and the identity

$$(4\pi L)^2\widehat{\mathcal{G}}_0(\vec{\mathbf{x}}, \vec{\mathbf{y}}, \omega)\overline{\widehat{\mathcal{G}}_0(\vec{\mathbf{x}}, \vec{\mathbf{y}}^\star, \omega)} = \exp\left[-\frac{ik}{L}\mathbf{x}\cdot\boldsymbol{\xi} + ik\eta\right], \tag{4.10}$$

for $\vec{\mathbf{y}} = (\boldsymbol{\xi}, L+\eta)$ and $\vec{\mathbf{x}} = (\mathbf{x}, 0)$, we get

$$\begin{aligned} (\mathcal{U}^*(\omega)\widehat{\Pi}_F(\omega)\mathcal{U}^*(\omega)f)(\mathbf{x}_r) = \frac{k^2}{(4\pi L)^2}\int_{\mathcal{A}} d\mathbf{x}_s f(\mathbf{x}_s)\int_{B\times L+[-h/2,h/2]} d\vec{\mathbf{y}} \\ \cdot\, \rho(\vec{\mathbf{y}})\exp\left[-\frac{ik}{L}(\mathbf{x}_r+\mathbf{x}_s)\cdot\boldsymbol{\xi} + 2ik\eta\right]. \end{aligned} \tag{4.11}$$

When the reflectivity is $\rho(\vec{\mathbf{y}}) = \chi_{\mathcal{B}}(\boldsymbol{\xi})\rho_L(\eta)$, the above expression simplifies to

$$(\mathcal{U}^*(\omega)\widehat{\Pi}_F(\omega)\mathcal{U}^*(\omega)f)(\mathbf{x}_r) = \frac{\widehat{\rho}_L(-2k)}{4}\frac{1}{(2\pi)^2}\int_{\mathcal{A}} d\mathbf{x}_s f(\mathbf{x}_s)\widehat{\chi}_{\frac{k}{L}\mathcal{B}}(\mathbf{x}_r+\mathbf{x}_s)\chi_{\mathcal{A}}(\mathbf{x}_r).$$

The result follows by identifying above the kernel representation of $Q_{\frac{k}{L}\mathcal{B}}$,

$$(Q_{\frac{k}{L}\mathcal{B}}f)(\mathbf{x}) = \frac{1}{(2\pi)^2}\int d\mathbf{y} f(\mathbf{y})\widehat{\chi}_{\frac{k}{L}\mathcal{B}}(\mathbf{y}-\mathbf{x}). \qquad \blacksquare$$

Example 4.3 (taken from [5]). In two dimensions when the array is linear $[-a/2, a/2]\times 0$ and we wish to image the slit $[-b/2, b/2]\times L + [-h/2, h/2]$ with unit reflectivity, the singular values of $\widehat{\Pi}_F(\omega)$ are $2\pi^2 k\,|\widehat{\rho}_L(-2k)|\,\nu_n(kab/(4L))$. Here $\nu_n(C)$, with $C = kab/(4L)$, are the singular values of the operator $\mathcal{P}[C] = P_{[-1,1]}Q_{[-C,C]}P_{[-1,1]}$ with kernel representation,

$$(\mathcal{P}[C]f)(x) = \int_{-1}^{1} dy f(y)\frac{\sin[C(x-y)]}{\pi(x-y)}.$$

Here $P_{[-1,1]}$ is the orthogonal projection that restricts functions to the interval $[-1,1]$, and $Q_{[-C,C]} = \mathcal{F}^{-1}P_{[-C,C]}\mathcal{F}$ is the orthogonal projection that restricts a function to $[-C,C]$ in frequency. The singular functions of this operator can be computed explicitly and are the prolate spheroidal wave functions, as was shown by Landau, Pollak, and Slepian (see [42, 30, 41]), so the singular values $\nu_n(C)$ are known analytically. The properties of this operator are considered further in Appendix A.

Therefore, in the Fraunhofer regime the array response $\widehat{\Pi}_F(\omega)$ is, up to unitary transformations, a space and wavenumber limiting operator. Let us now review properties of this class of operators.

4.5. Space and wavenumber limiting. The problem of finding a function localized to some set $\mathcal{A}$ (in space) and whose Fourier transform is most concentrated on another set $\mathcal{B}$ can be solved with the spectral decomposition of the operator $\mathcal{A}Q_{\mathcal{B}}\mathcal{A}$. When $\mathcal{A}$ and $\mathcal{B}$ are intervals of the real line, this problem has an explicit solution in terms of the prolate spheroidal wave functions, as was shown by Slepian and Pollak [42] (see also [40]). One of the many generalizations (see, e.g., the review by Slepian [41]) of their work is to higher dimensions. We review known results about the generalized prolate spheroidal wave functions that allow us to analyze the behavior of our imaging algorithm. Because of our problem setup, we limit the discussion to two-dimensional versions of results that also hold in higher dimensions.

4.5.1. Space and wavenumber limited functions. A function f that is supported on a set $\mathcal{A}$ in space is such that $f = \mathcal{A}f$, so its L^2 norm is $\|\mathcal{A}f\|^2$ or, by Parseval's identity, $(2\pi)^{-2}\|\mathcal{F}\mathcal{A}f\|^2$. Now the norm of f measured on the set $\mathcal{B}$ in the Fourier domain is $(2\pi)^{-2}\|\mathcal{B}\mathcal{F}\mathcal{A}f\|^2$. Functions that are restricted to the set $\mathcal{A}$ and that are well localized on the set $\mathcal{B}$ in Fourier space maximize the ratio

$$(2\pi)^{-2}\frac{\|\mathcal{B}\mathcal{F}\mathcal{A}f\|^2}{\|\mathcal{A}f\|^2} = (2\pi)^{-2}\frac{\langle \mathcal{B}\mathcal{F}\mathcal{A}f, \mathcal{B}\mathcal{F}\mathcal{A}f\rangle}{\langle f, f\rangle}, \tag{4.12}$$

where $\langle \cdot, \cdot \rangle$ is the usual $L^2(\mathbb{R}^2)$ inner product and we have $f = \mathcal{A}f$. The ratio (4.12) is the Rayleigh quotient for the self-adjoint operator $(2\pi)^{-2}\mathcal{A}\mathcal{F}^*\mathcal{B}\mathcal{F}\mathcal{A} = \mathcal{A}Q_{\mathcal{B}}\mathcal{A}$, since $Q_{\mathcal{B}} = \mathcal{F}^{-1}\mathcal{B}\mathcal{F}$ and $\mathcal{F}^{-1} = (2\pi)^{-2}\mathcal{F}^*$. Since $\mathcal{A}Q_{\mathcal{B}}\mathcal{A}$ is compact, the concentration in energy (4.12) is maximized by the eigenfunction $v_1[\mathcal{A}Q_{\mathcal{B}}\mathcal{A}]$ corresponding to the largest eigenvalue $\sigma_1[\mathcal{A}Q_{\mathcal{B}}\mathcal{A}]$. The compactness of $\mathcal{A}Q_{\mathcal{B}}\mathcal{A}$ follows from it being of trace class, since by Mercer's theorem,

$$\operatorname{tr} \mathcal{A}Q_{\mathcal{B}}\mathcal{A} = \sum_j \sigma_j[\mathcal{A}Q_{\mathcal{B}}\mathcal{A}] = \frac{1}{(2\pi)^2}\int d\mathbf{x}\chi_{\mathcal{A}}(\mathbf{x})\chi_{\mathcal{A}}(\mathbf{x})\widehat{\chi}_{\mathcal{B}}(\mathbf{x}-\mathbf{x}) = \frac{|\mathcal{A}|\,|\mathcal{B}|}{(2\pi)^2},$$

where $|\cdot|$ denotes the area (measure) of a set.

We could have formulated the problem differently: what is the function localized in the Fourier domain to $\mathcal{B}$, that is most concentrated in space to $\mathcal{A}$? The answer is the eigenfunction of $\mathcal{B}Q^*_{\mathcal{A}}\mathcal{B} = \mathcal{B}\mathcal{F}\mathcal{A}\mathcal{F}^{-1}\mathcal{B}$ with largest eigenvalue. From this reformulation we see that the Fourier transform of an eigenfunction, $\mathcal{F}v[\mathcal{A}Q_{\mathcal{B}}\mathcal{A}]$, is a function of the same form, $v[Q_{\mathcal{A}}\mathcal{B}Q_{\mathcal{A}}]$. This important property of essential invariance under Fourier transforms is used in Proposition 4.5.

So far we have effectively constructed the left and right singular functions of the operator $(2\pi)^{-1}\mathcal{B}\mathcal{F}\mathcal{A}$ with largest singular value (we omit the $(2\pi)^{-1}$ factor when referring to singular functions). The remaining singular functions solve constrained problems: the jth right singular function $v_j[\mathcal{B}\mathcal{F}\mathcal{A}]$ maximizes the concentration (4.12) while being orthogonal to the first $j-1$ right singular functions, and the jth left singular function $u_j[\mathcal{B}\mathcal{F}\mathcal{A}]$ is the function localized in frequency domain to $\mathcal{B}$ that is most concentrated in space to $\mathcal{A}$ and orthogonal to the first $j-1$ left singular functions.

4.5.2. Asymptotics of the eigenvalue distribution. A remarkable result about the spectrum of $\mathcal{A}Q_{\mathcal{B}}\mathcal{A}$ is that for large sets $\mathcal{B}$, this product of orthogonal projections behaves itself like an orthogonal projection: its higher $(2\pi)^{-2}|\mathcal{A}|\,|\mathcal{B}|$ eigenvalues are close to one and then plunge to zero very rapidly. For the operator $\mathcal{A}Q_{\frac{k}{L}\mathcal{B}}\mathcal{A}$ that we encountered in our study of the array response $\widehat{\Pi}_F(\omega)$, this result can be seen as a large Fresnel number $\theta_{ab} = kab/L$ asymptotic form of its eigenvalue distribution function, where a is the size of the array and b that of the target, in cross-range. The eigenvalue distribution of $\mathcal{A}Q_{\frac{k}{L}\mathcal{B}}\mathcal{A}$ is defined by

$$N(\delta;\theta_{ab}) = \#\left\{ j \mid \sigma_j[\mathcal{A}Q_{\frac{k}{L}\mathcal{B}}\mathcal{A}] > \delta \right\} \quad \text{for } 0 < \delta < 1.$$

That the operator $\mathcal{A}Q_{\frac{k}{L}\mathcal{B}}\mathcal{A}$ behaves like an orthogonal projection can be seen by applying the results of Kac, Murdock, and Szegő [24] on Hermitian Toeplitz operators (see also Landau [29] for a direct proof). As $\theta_{ab} \to \infty$ we have the asymptotic form

$$N(\delta;\theta_{ab}) = (\lambda L)^{-2}|\mathcal{A}|\,|\mathcal{B}|\,(1+o(1)), \tag{4.13}$$

where the leading term is $\mathcal{O}(\theta_{ab}^2)$. To first order, $N(\delta;\theta_{ab})$ is independent of δ, which means that the first $(\lambda L)^{-2}|\mathcal{A}|\,|\mathcal{B}|$ eigenvalues are close to one, while the rest are close to zero. This phenomenon has been seen in actual experiments (see, e.g., [44, 43]) since the first term in the expansion can be rewritten as

$$N(\delta;\theta_{ab}) \approx \frac{|\mathcal{B}|}{(\lambda L)^2/|\mathcal{A}|};$$

that is, the rank of the array data operator produced by the target is roughly equal to the number of focal spot areas (square of the spot size) that fit in the target.

In the numerical simulations of section 3 we are in a scaling regime that is different from the Fraunhofer regime, and so we do not observe this law or the plateau. The computed singular values decay faster than they would in the Fraunhofer regime, as can be seen in Figure 14. This significant difference in the distribution of eigenvalues is explained in section 5 by analyzing the response matrix in an extended Fraunhofer regime.

Remark 4.4. In our imaging method we migrate the singular functions of $\widehat{\Pi}(\omega)$ for singular values, rescaled by $\sigma_1[\widehat{\Pi}(\omega)]$, in some interval $[\alpha, \beta] \subset (0, 1)$. By the above result on the distribution of eigenvalues, $\sigma_1[\mathcal{A}Q_{\frac{k}{L}\mathcal{B}}\mathcal{A}] \approx 1$. Thus by dividing all the singular values of $\widehat{\Pi}(\omega)$ by $\sigma_1[\widehat{\Pi}(\omega)]$ we cancel out the effect on the singular values of the range dimension of the target, that is, the factor $|\widehat{\rho}(-2k)|/4$ in Proposition 4.2, and recover the singular values of the underlying operator $\mathcal{A}Q_{\frac{k}{L}\mathcal{B}}\mathcal{A}$.

The singular values in the plunge region (intermediate) of $\mathcal{A}Q_{\frac{k}{L}\mathcal{B}}\mathcal{A}$ are the ones we use to illuminate the edges of the target (see section 3). However, the asymptotic form (4.13) indicates that the width of the plunge region is relatively small as $\theta_{ab} \to \infty$; it does not give any information other than that it is $o(\theta_{ab}^2)$.

Next we review refinements of (4.13) that quantify the width of the plunge region.

4.5.3. Second order asymptotics of the eigenvalue distribution. For Hermitian operators $T_r : L^2(\mathcal{A}') \to L^2(\mathcal{A}')$ of the form

$$(T_r u)(\mathbf{x}) = \frac{r^2}{(2\pi)^2} \int_{\mathcal{A}'} d\mathbf{y} u(\mathbf{y}) \int_{\mathbb{R}^2} d\boldsymbol{\xi} \exp[ir\boldsymbol{\xi} \cdot (\mathbf{x} - \mathbf{y})] q(\mathbf{x}, \boldsymbol{\xi})$$

with real symbol $q(\mathbf{x}, \boldsymbol{\xi})$ and having jump type discontinuities in $\boldsymbol{\xi}$, Widom [49, 50] conjectured a second order asymptotic formula for computing tr $f(T_r)$ for suitable functions f, as the dilation factor $r \to \infty$. The operator $\mathcal{A}Q_{\frac{k}{L}\mathcal{B}}\mathcal{A}$ is precisely in this class: its symbol is $q(\mathbf{x}, \boldsymbol{\xi}) = \chi_{b^{-1}\mathcal{B}}(\boldsymbol{\xi})$, $\mathcal{A}' = a^{-1}\mathcal{A}$ and the dilation factor is the Fresnel number $r = \theta_{ab} = kab/L$. Moreover, knowing the large θ_{ab} asymptotics for tr $f(\mathcal{A}Q_{\frac{k}{L}\mathcal{B}}\mathcal{A})$ automatically gives an asymptotic form for $N(\delta; \theta_{ab})$ since

$$N(\delta; \theta_{ab}) = \int_\delta^1 dt \frac{d}{dt}[-N(t; \theta_{ab})] = \text{tr } \chi_{(\delta,1)}(\mathcal{A}Q_{\frac{k}{L}\mathcal{B}}\mathcal{A}).$$

Assuming that the Widom asymptotic expansion holds, we have

$$\begin{aligned} N(\delta; \theta_{ab}) &= (\lambda L)^{-2} |\mathcal{A}| |\mathcal{B}| \\ &\quad + (\lambda L)^{-1} \frac{\ln \theta_{ab}}{4\pi^2} \ln \frac{1-\delta}{\delta} \int_{\partial\mathcal{A}} \int_{\partial\mathcal{B}} d\mathbf{x} d\boldsymbol{\xi} \, |\mathbf{n}_{\mathcal{A}}(\mathbf{x}) \cdot \mathbf{n}_{\mathcal{B}}(\boldsymbol{\xi})| \\ &\quad + o(\theta_{ab} \ln \theta_{ab}). \end{aligned} \tag{4.14}$$

The Widom conjecture has been shown to hold in one dimension by Landau and Widom [31], and in higher dimensions when the domain $\mathcal{B}$ is a half-space [50]. Gioev [19] has recently confirmed that the second term in the asymptotics of tr $f(T_r)$ is of the order predicted by

Widom. In Appendix A we show that (4.14) holds in the very particular case of rectangular $\mathcal{A}$ and $\mathcal{B}$ using the one-dimensional two-term asymptotics [31].

The expansion (4.14) indicates that information about the edges of $\mathcal{B}$ appears redundantly in the plunge region. Indeed, if the Widom conjecture holds, then the number of eigenvalues in the plunge region is proportional to the double integral term, which is less than the product $|\partial\mathcal{A}|\,|\partial\mathcal{B}|$ of the perimeters of $\mathcal{A}$ and $\mathcal{B}$. This is probably why similar edge images can be obtained with different parts of the plunge region, as we see in the numerical simulations of section 3, with selected subspace migration.

Another use of the large Fresnel number asymptotic expression (4.14) could be for detecting edges by looking at the rate of decay in the plunge region. Indeed, if the reflectivity in the cross-range dimension is smooth, the second term would be only $\mathcal{O}(\theta_{ab})$ (see, e.g., [47, 48]), instead of being $\mathcal{O}(\theta_{ab}\ln\theta_{ab})$ as it is in (4.14).

4.5.4. Localization of the singular functions. The leading singular function $v_1[(\frac{k}{L}\mathcal{B})\mathcal{F}\mathcal{A}]$ peaks typically at the center of $\mathcal{A}$ and dies off quickly away from its peak. The corresponding left singular function $u_1[(\frac{k}{L}\mathcal{B})\mathcal{F}\mathcal{A}]$ behaves similarly in $\frac{k}{L}\mathcal{B}$. As j increases, the peaks of the singular functions move progressively outward to the edges of their respective domain, with oscillations that die off quickly away from the peaks.

The singular value $\sigma_j[\mathcal{A}Q_{\frac{k}{L}\mathcal{B}}\mathcal{A}]$ measures the fraction of energy in $\mathcal{A}$ (resp., $\frac{k}{L}\mathcal{B}$) of the extension of $v_j[(\frac{k}{L}\mathcal{B})\mathcal{F}\mathcal{A}]$ (resp., $u_j[(\frac{k}{L}\mathcal{B})\mathcal{F}\mathcal{A}]$) to $L^2(\mathbb{R}^2)$. Slepian [38] defines the extension of $v_j[(\frac{k}{L}\mathcal{B})\mathcal{F}\mathcal{A}]$ by

$$v_j[(\tfrac{k}{L}\mathcal{B})\mathcal{F}\mathcal{A}](\mathbf{x}) = \frac{1}{\sigma_j[\mathcal{A}Q_{\frac{k}{L}\mathcal{B}}\mathcal{A}]}(2\pi)^{-2}\int_{\mathcal{A}} d\mathbf{y}\, v_j[(\tfrac{k}{L}\mathcal{B})\mathcal{F}\mathcal{A}](\mathbf{y})\widehat{\chi}_{\frac{k}{L}\mathcal{B}}(\mathbf{y}-\mathbf{x}) \quad \text{for } \mathbf{x}\in\mathbb{R}^2. \tag{4.15}$$

In addition to being orthonormal in $L^2(\mathcal{A})$, the extended functions have the property of being mutually orthogonal also in $L^2(\mathbb{R}^2)$ with $\langle v_i, v_j\rangle = \delta_{i,j}/\sigma_i[\mathcal{A}Q_{\frac{k}{L}\mathcal{B}}\mathcal{A}]$. The domain of definition of the left singular functions can be similarly extended from $\frac{k}{L}\mathcal{B}$ to $\mathbb{R}^2$.

We know that roughly the first $(\lambda L)^{-2}\,|\mathcal{A}|\,|\mathcal{B}|$ singular values of $\mathcal{A}Q_{\frac{k}{L}\mathcal{B}}\mathcal{A}$ are close to one. Therefore, the first $(\lambda L)^{-2}\,|\mathcal{A}|\,|\mathcal{B}|$ singular functions $u_j[(\frac{k}{L}\mathcal{B})\mathcal{F}\mathcal{A}]$ are relatively well concentrated inside $\frac{k}{L}\mathcal{B}$. The situation is exactly the opposite for singular values with index above the threshold. Therefore, if we want singular functions that peak on the edges of $\frac{k}{L}\mathcal{B}$, we should consider the plunge region, which corresponds to intermediate singular values.

The localization property of the eigenfunctions of the response matrix has been observed experimentally [26]. To further illustrate localization, we give in Appendix A explicit formulas for the singular functions of $\mathcal{B}\mathcal{F}\mathcal{A}$ when both $\mathcal{A}$ and $\mathcal{B}$ are rectangles. Also, the fact that the images in range agree with $\partial\mathcal{B}$ for other cross-range profiles $\mathcal{B}$ indicates that this localization property holds more generally.

In the next section 4.6 we show that the single-frequency, single-eigenfunction subspace migration image (2.2) is roughly $\left|u_j[(\frac{k}{L}\mathcal{B})\mathcal{F}\mathcal{A}](\frac{k}{L}\cdot)\right|^2$. Therefore, the localization property explains why we can focus on the edges by imaging with the singular functions in the plunge region.

4.6. Analysis of selected subspace migration. In this section we connect the subspace migration images to the singular functions of space and wavenumber limiting operators. We express the image resulting from migrating a right singular function of $\widehat{\Pi}_F(\omega)$ in terms of the left singular functions of $(\frac{k}{L}\mathcal{B})\mathcal{F}\mathcal{A}$. We present this result as Proposition 4.5. It allows us to apply the properties of the SVD of space and frequency limiting operators to explain the behavior of selected subspace imaging in the numerical simulations of section 3.

Proposition 4.5. *Subspace migration images* (2.2) *with a single singular function* $v_j[\widehat{\Pi}_F(\omega)]$ *at a single frequency* ω *in the Fraunhofer regime have the form*

$$\mathcal{I}_{\mathrm{SM}}(\vec{\mathbf{y}}^S;\omega) \sim \overline{\widehat{\rho}_L(-2k)}\exp[2ik\eta^S]\sigma_j^2[\mathcal{A}Q_{\frac{k}{L}\mathcal{B}}\mathcal{A}]\left|u_j\left[\left(\frac{k}{L}\mathcal{B}\right)\mathcal{F}\mathcal{A}\right]\left(\frac{k}{L}\boldsymbol{\xi}^S\right)\right|^2,$$

where the search point is $\vec{\mathbf{y}}^S = (\boldsymbol{\xi}^S, L+\eta^S)$ *and the symbol* $\sim$ *means equality up to a positive multiplicative factor, independent of* ω, j, *and* $\vec{\mathbf{y}}^S$. *Here the values of* $u_j[(\frac{k}{L}\mathcal{B})\mathcal{F}\mathcal{A}]$ *outside* $\frac{k}{L}\mathcal{B}$ *are given by Slepian's extension* (4.15).

This result shows that images with subspace selection are as localized as the left singular functions of $(\frac{k}{L}\mathcal{B})\mathcal{F}\mathcal{A}$. By section 4.5.4, the singular functions for intermediate singular values are localized near the edges of the array and the object. Thus, when we migrate with a subspace that contains those intermediate singular functions we expect to image the edges with illuminations coming mainly from the edges of the array. This agrees with the numerical simulations of section 3.

When the single frequency image is summed over the frequencies, the simulation results in section 3 indicate that the oscillatory part (recall section 4.5.4) of the singular functions average out.

The potential for imaging with eigenfunctions has been noted in [35, 33] for the full aperture, far field operator, which is different from array imaging. In array imaging the selective focusing on the edges with illuminations coming from the ends of a linear array was shown in [5].

Proof of Proposition 4.5. Using the continuum approximation of the $\mathbb{C}^N$ inner product, which is the $L^2(\mathcal{A})$ inner product, the subspace migration imaging functional (2.2) for a single singular function becomes

$$\mathcal{I}_{\mathrm{SM}}(\vec{\mathbf{y}}^S;\omega) \sim \int_{\mathcal{A}} d\mathbf{x}_r \int_{\mathcal{A}} d\mathbf{x}_s \exp\left[ik\left|\vec{\mathbf{x}}_r - \vec{\mathbf{y}}^S\right| + ik\left|\vec{\mathbf{x}}_s - \vec{\mathbf{y}}^S\right|\right]$$
$$\cdot\, \overline{\sigma_j[\widehat{\Pi}_F(\omega)]u_j[\widehat{\Pi}_F(\omega)](\mathbf{x}_r)v_j^*[\widehat{\Pi}_F(\omega)](\mathbf{x}_s)}.$$

Here the symbol $\sim$ means equality up to a positive multiplicative factor. From Proposition 4.2 and approximating the phases in the complex exponentials as in (4.7) we obtain

$$\mathcal{I}_{\mathrm{SM}}(\vec{\mathbf{y}}^S;\omega) \sim \overline{\widehat{\rho}_L(-2k)}\sigma_j' \int_{\mathcal{A}} d\mathbf{x}_r \int_{\mathcal{A}} d\mathbf{x}_s \widehat{\mathcal{G}}_0(\vec{\mathbf{x}}_r, \vec{\mathbf{y}}^S, \omega)\widehat{\mathcal{G}}_0(\vec{\mathbf{x}}_s, \vec{\mathbf{y}}^S, \omega)$$
$$\cdot\, \overline{\widehat{\mathcal{G}}_0(\vec{\mathbf{x}}_r, \vec{\mathbf{y}}^\star, \omega)v_j'(-\mathbf{x}_r)\widehat{\mathcal{G}}_0(\vec{\mathbf{x}}_s, \vec{\mathbf{y}}^\star, \omega)\overline{v_j'(\mathbf{x}_s)}},$$

where to simplify the notation we write $v_j' \equiv v_j[(\frac{k}{L}\mathcal{B})\mathcal{F}\mathcal{A}]$ and $\sigma_j' \equiv \sigma_j[\mathcal{A}Q_{\frac{k}{L}\mathcal{B}}\mathcal{A}]$. Recalling the expression (4.7) of $\widehat{\mathcal{G}}_0$ and that $\vec{\mathbf{y}}^S \equiv (\boldsymbol{\xi}^S, L+\eta^S)$, we obtain

$$\mathcal{I}_{\rm SM}(\vec{\mathbf{y}}^S;\omega) \sim \overline{\widehat{\rho}_L(-2k)}\sigma_j' \int_{\mathcal{A}} d\mathbf{x}_r \int_{\mathcal{A}} d\mathbf{x}_s \exp\left[2ik\eta^S - \frac{ik}{L}(\mathbf{x}_r+\mathbf{x}_s)\cdot\boldsymbol{\xi}^S\right] \overline{v_j'(-\mathbf{x}_r)} v_j'(\mathbf{x}_s),$$

which becomes (using Fubini's theorem)

$$\mathcal{I}_{\rm SM}(\vec{\mathbf{y}}^S;\omega) \sim \frac{\overline{\widehat{\rho}_L(-2k)}}{4}\exp[2ik\eta^S]\sigma_j' \left(\int_{\mathcal{A}} d\mathbf{x}_r \exp\left[-\frac{ik}{L}\mathbf{x}_r\cdot\boldsymbol{\xi}^S\right]\overline{v_j'(-\mathbf{x}_r)}\right) \left(\int_{\mathcal{A}} d\mathbf{x}_s \exp\left[-\frac{ik}{L}\mathbf{x}_s\cdot\boldsymbol{\xi}^S\right] v_j'(\mathbf{x}_s)\right).$$

We have assumed here that the set $\mathcal{A}$ is symmetric about the origin ($\mathbf{x}\in\mathcal{A} \Leftrightarrow -\mathbf{x}\in\mathcal{A}$). Therefore

$$\mathcal{I}_{\rm SM}(\vec{\mathbf{y}}^S;\omega) \sim \overline{\widehat{\rho}_L(-2k)}\exp[2ik\eta^S]\sigma_j' \left|(\mathcal{F}\mathcal{A}v_j')\left(\frac{k}{L}\boldsymbol{\xi}^S\right)\right|^2.$$

Finally, from the definition of the SVD we have

$$\left(\frac{k}{L}\mathcal{B}\right)\mathcal{F}\mathcal{A}v_j' = \sigma_j\left[\left(\frac{k}{L}\mathcal{B}\right)\mathcal{F}\mathcal{A}\right]u_j' = 2\pi\sqrt{\sigma_j'}u_j', \tag{4.16}$$

where $u_j' \equiv u_j[(\frac{k}{L}\mathcal{B})\mathcal{F}\mathcal{A}]$. In one dimension, property (4.16) is the remarkable self-similarity of the prolate spheroidal wave functions with respect to the Fourier transform [41], noted in section 4.5.1. Here, it translates into knowing the field at the target after migration from the array. Thus, the image *inside* the cross-section $\mathcal{B}$ of the target takes the form

$$\mathcal{I}_{\rm SM}(\vec{\mathbf{y}}^S;\omega) \sim \overline{\widehat{\rho}_L(-2k)}\exp[2ik\eta^S]\sigma_j'^2 \left|u_j'\left(\frac{k}{L}\boldsymbol{\xi}^S\right)\right|^2 \quad \text{for } \boldsymbol{\xi}^S\in\mathcal{B}. \tag{4.17}$$

Outside $\mathcal{B}$ the image is also given by (4.17), provided Slepian's extension (4.15) of u_j' is used. This is because the extension of u_j' that is naturally defined by (4.16)

$$g_j'(\boldsymbol{\zeta}) = \frac{1}{2\pi(\sigma_j')^{1/2}}\int_{\mathcal{A}} d\mathbf{x}\exp\left[-i\mathbf{x}\cdot\boldsymbol{\zeta}\right]v_j'(\mathbf{x}), \quad \text{for } \boldsymbol{\zeta}\in\mathbb{R}^2, \tag{4.18}$$

is equivalent to (4.15). To see this, simply substitute v_j' above by using the properties of the SVD: $v_j' = (\sigma_j\left[\left(\frac{k}{L}\mathcal{B}\right)\mathcal{F}\mathcal{A}\right])^{-1}\mathcal{A}\mathcal{F}^*(\frac{k}{L}\mathcal{B})u_j'$, to obtain after some manipulations

$$g_j'(\boldsymbol{\zeta}) = \frac{1}{(2\pi)^2\sigma_j'}\int_{\frac{k}{L}\mathcal{B}} d\boldsymbol{\zeta}' u_j'(\boldsymbol{\zeta}')\widehat{\chi}_{\mathcal{A}}(\boldsymbol{\zeta}'-\boldsymbol{\zeta})$$

which for $\mathcal{A}$ symmetric about the origin is precisely Slepian's extension (4.15). ■

5. The extended Fraunhofer regime. In the analysis of imaging in the Fraunhofer regime in section 4 we assume that the target is small ($\theta_b \ll 1$). However, in the numerical simulations we violate this condition, since we have $\theta_b = 8\pi$. Although the qualitative behavior of our imaging algorithm can be understood using the analysis of the Fraunhofer regime, quantitatively the story is different. Figure 14 shows that there is a significant difference between the computed singular values and those predicted by the Fraunhofer regime. We now introduce an extended Fraunhofer regime that accounts for this discrepancy by incorporating $\theta_b \geq 1$ in the analysis of sections 4.3 and 4.4. Preliminary results suggest a scaling law analogous to (4.13).

5.1. The array response matrix in the extended Fraunhofer regime. We proceed as in section 4.3 to approximate the array response matrix $\widehat{\Pi}(\vec{\mathbf{x}}_r, \vec{\mathbf{x}}_s, \omega)$ for large targets. We make the Born and the paraxial approximation $\widehat{\mathcal{G}}_0^{\mathrm{Fre}}$ of the Green's function to get

$$\widehat{\Pi}(\vec{\mathbf{x}}_r, \vec{\mathbf{x}}_s, \omega) \approx \widehat{\Pi}_{\mathrm{Fre}}(\vec{\mathbf{x}}_r, \vec{\mathbf{x}}_s, \omega) = k^2 \int_{\mathcal{B}\times L+[-h/2,h/2]} d\vec{\mathbf{y}} \rho(\vec{\mathbf{y}}) \widehat{\mathcal{G}}_0^{\mathrm{Fre}}(\vec{\mathbf{x}}_r, \vec{\mathbf{y}}, \omega) \widehat{\mathcal{G}}_0^{\mathrm{Fre}}(\vec{\mathbf{x}}_s, \vec{\mathbf{y}}, \omega).$$

For large targets the difference is that the approximation (4.7) of the free space Green's function is not valid because we neglected an $\mathcal{O}(\theta_b)$ term in the phase. When we include this term the new approximation to the Green's function is

$$\widehat{G}_0(\vec{\mathbf{x}}, \vec{\mathbf{y}}, \omega) \approx \widehat{\mathcal{G}}_0^{\mathrm{Fre}}(\vec{\mathbf{x}}, \vec{\mathbf{y}}, \omega) = \frac{1}{4\pi L} \exp\left[ik\left(L + \eta + \frac{|\mathbf{x}|^2}{2L} - \frac{\mathbf{x}\cdot\boldsymbol{\xi}}{L} + \frac{|\boldsymbol{\xi}|^2}{2L}\right)\right] \tag{5.1}$$

for $\vec{\mathbf{x}} = (\mathbf{x}, 0)$ in the array and $\vec{\mathbf{y}} = (\boldsymbol{\xi}, L + \eta)$ in the vicinity of the target. The additional term in the phase appears in the study of Fresnel diffraction [8], which explains our notation $\widehat{\Pi}_{\mathrm{Fre}}(\vec{\mathbf{x}}_r, \vec{\mathbf{x}}_s, \omega)$.

5.2. The singular value decomposition of the response matrix in the extended Fraunhofer regime. We give a characterization analogous to Proposition 4.1 for the operator $\widehat{\Pi}_{\mathrm{Fre}}(\omega) : L^2(\mathcal{A}) \to L^2(\mathcal{A})$ defined by

$$(\widehat{\Pi}_{\mathrm{Fre}}(\omega) f)(\mathbf{x}) = \int_{\mathcal{A}} d\mathbf{y} f(\mathbf{y}) \widehat{\Pi}_{\mathrm{Fre}}((\mathbf{x}, 0), (\mathbf{y}, 0), \omega),$$

when the reflectivity is of the form $\rho(\vec{\mathbf{y}}) = \chi_{\mathcal{B}}(\boldsymbol{\xi})\rho_L(\eta)$. We omit the proof since it goes along the same lines as the proof of Proposition 4.1.

Proposition 5.1. *When the array is invariant with respect to reflections about the origin ($-\mathbf{x} \in \mathcal{A} \Leftrightarrow \mathbf{x} \in \mathcal{A}$), we have*

$$\widehat{\Pi}_{\mathrm{Fre}}(\omega) = \frac{\widehat{\rho}_L(-2k)}{4} \mathcal{U}(\omega) \mathcal{R} \mathcal{A} \widetilde{Q}_{\frac{k}{L}\mathcal{B}} \mathcal{A} \mathcal{U}(\omega).$$

Here $\mathcal{U}(\omega)$, $\mathcal{R}$, and $\mathcal{A}$ are operators identical to those appearing in Proposition 4.1. The operator $\widetilde{Q}_{\frac{k}{L}\mathcal{B}}$ is a non-Hermitian one with kernel representation,

$$(\widetilde{Q}_{\frac{k}{L}\mathcal{B}} f)(\mathbf{x}) = (2\pi)^{-2} \int d\mathbf{y} f(\mathbf{y}) \widehat{q}(\mathbf{y} - \mathbf{x}), \quad \text{where} \quad q(\boldsymbol{\xi}) = \chi_{\frac{k}{L}\mathcal{B}}(\boldsymbol{\xi}) \exp\left[i \frac{L}{k} |\boldsymbol{\xi}|^2\right].$$

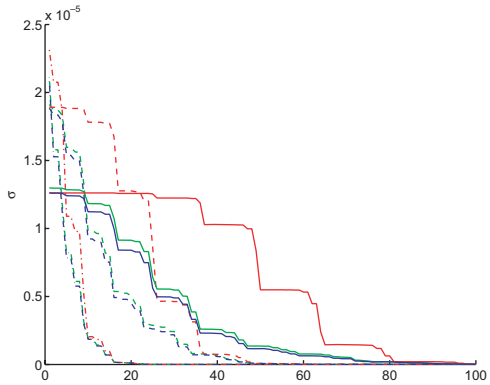

Figure 14. *The computed (green lines) singular values of the array response matrix versus the ones predicted in the usual (red lines) and extended (blue lines) Fraunhofer regimes for a rectangular target, and for frequencies* $1.5MHz$ *(-·-),* $3MHz$ *(- -), and* $4.5MHz$ *(—). The singular values in the extended Fraunhofer regime are obtained from* (5.2) *using* $k = 2\pi/\lambda$, $L = 100\lambda_0$, $a = 24.5\lambda_0$, *and* $b = 20\lambda_0$, *which are the same as those in section* 3.

However, the operator $\mathcal{A}\widetilde{Q}_{\frac{k}{L}\mathcal{B}}\mathcal{A}$ is still Hilbert–Schmidt. This can be seen by comparing with Example X.2.2 in [51] and

$$\int_{\mathcal{A}}\int_{\mathcal{A}} d\mathbf{x}d\mathbf{y}\,|\widehat{q}(\mathbf{x}-\mathbf{y})|^2 < \infty.$$

Thus the SVD of $\mathcal{A}\widetilde{Q}_{\frac{k}{L}\mathcal{B}}\mathcal{A}$ is well defined. The SVD of $\widehat{\Pi}_{\rm Fre}(\omega)$ follows from a result similar to Proposition 4.2.

Proposition 5.2. *The singular values of* $\widehat{\Pi}_{\rm Fre}(\omega)$ *are for* $n \in \mathbb{N}$

$$\sigma_n[\widehat{\Pi}_{\rm Fre}(\omega)] = \frac{|\widehat{\rho}_L(-2k)|}{4}\sigma_n[\mathcal{A}\widetilde{Q}_{\frac{k}{L}\mathcal{B}}\mathcal{A}],$$

with associated right and left singular functions

$$v_n[\widehat{\Pi}_{\rm Fre}(\omega)] = \mathcal{U}^*(\omega)v_n[\mathcal{A}\widetilde{Q}_{\frac{k}{L}\mathcal{B}}\mathcal{A}] \quad \textit{and}$$
$$u_n[\widehat{\Pi}_{\rm Fre}(\omega)] = \arg(\widehat{\rho}_L(-2k))\mathcal{U}(\omega)\mathcal{R}u_n[\mathcal{A}\widetilde{Q}_{\frac{k}{L}\mathcal{B}}\mathcal{A}].$$

Therefore, up to unitary transformations, the array response matrix in the extended Fraunhofer regime is the operator $\mathcal{A}\widetilde{Q}_{\frac{k}{L}\mathcal{B}}\mathcal{A}$.

5.2.1. Comparison with the Fraunhofer regime. We compare in Figure 14 the singular values of the array response matrix for a square $20\lambda_0 \times 20\lambda_0$ target to the singular values predicted by the usual and the extended Fraunhofer regimes. The singular values of $\mathcal{A}Q_{\frac{k}{L}\mathcal{B}}\mathcal{A}$ (usual Fraunhofer regime) can be computed analytically using the one-dimensional prolate spheroidal wave functions (see Appendix A). As for the singular values of $\mathcal{A}\widetilde{Q}_{\frac{k}{L}\mathcal{B}}\mathcal{A}$ (extended Fraunhofer regime), we obtain them similarly using separation of variables from the singular values of its analogous one-dimensional operator

$$(2\pi)^{-1}\int_{-a/2}^{a/2} dy f(y)\widehat{q}(y-x), \quad \text{where} \quad q(\xi) = \chi_{\frac{k}{L}[-b/2,b/2]}(\xi)\exp\left[i\frac{L}{k}\xi^2\right], \tag{5.2}$$

which we approximate using collocation. In Appendix A, the eigenfunctions of the operator (5.2) are compared to those that would be obtained in the usual Fraunhofer regime when $q(\xi) = \chi_{\frac{k}{L}[-b/2,b/2]}(\xi)$ in (5.2).

5.3. Distribution result for the pseudospectrum. The operator $\mathcal{A}\widetilde{Q}_{\frac{k}{L}\mathcal{B}}\mathcal{A}$ is non-Hermitian, so we cannot speak about eigenvalues and eigenvectors since their existence is not guaranteed. Landau [29] was among the first proponents of pseudospectra for the study of non-Hermitian operators [45], and one of his original results gives a scaling law that is similar in spirit to the one in the Fraunhofer regime (4.13).

An ε-pseudoeigenvalue $\mu \in \mathbb{C}$ of $\mathcal{A}\widetilde{Q}_{\frac{k}{L}\mathcal{B}}\mathcal{A}$ is such that

$$\left\| \mathcal{A}\widetilde{Q}_{\frac{k}{L}\mathcal{B}}\mathcal{A}\phi - \mu\phi \right\| \leq \varepsilon \quad \text{for some nonzero } \phi.$$

The function ϕ is said to be an ε-pseudoeigenfunction of $\mathcal{A}\widetilde{Q}_{\frac{k}{L}\mathcal{B}}\mathcal{A}$. Here we have used the $L^2(\mathcal{A})$ norm. In our setting, Theorem 3 in [29] means that the maximum number of orthogonal ε-pseudoeigenfunctions with ε-pseudoeigenvalues in the annulus[2]

$$\Omega = \{z \in \mathbb{C} \mid \delta \leq |z| \leq 1\}$$

is $(\lambda L)^{-2}\,|\mathcal{A}|\,|\Omega_{\mathcal{B}}|$, in the limit $\varepsilon \to 0$ and $\theta_{ab} \to \infty$. Here $\Omega_{\mathcal{B}}$ is the set of points for which the symbol of $\mathcal{A}\widetilde{Q}_{\frac{k}{L}\mathcal{B}}\mathcal{A}$ belongs to the annulus Ω, that is,

$$\Omega_{\mathcal{B}} = \{\boldsymbol{\xi} \in \mathbb{R}^2 \mid \chi_{\mathcal{B}}(\boldsymbol{\xi}) \exp[i(L/k)\,|\boldsymbol{\xi}|^2] \in \Omega\} = \mathcal{B}.$$

The last equality shows that in fact $\Omega_{\mathcal{B}}$ is the same as the set $\mathcal{B}$.

A physical interpretation (from Proposition 5.1) is that the maximal number of orthogonal (independent) signals f for which

$$\left\| \widehat{\Pi}_{\mathrm{Fre}}(\omega) f - \mu \frac{\widehat{\rho}_L(-2k)}{4} \mathcal{U}(\omega)\mathcal{R}\mathcal{U}(\omega) f \right\| \leq \varepsilon \quad \text{for some } \mu \in \mathbb{C} \text{ with } \delta \leq |\mu| \leq 1$$

is roughly $(\lambda L)^{-2}\,|\mathcal{A}|\,|\mathcal{B}|$ (the number of focal spot areas fitting in the target). In other words, there are about $|\mathcal{B}|\,/((\lambda L)^2/\,|\mathcal{A}|)$ orthogonal signals that when sent by the array, produce an echo which is essentially the same signal up to a reflection and a phase.

6. Summary and conclusions. We have introduced a selective subspace migration approach for array imaging of the edges of extended reflectors in homogeneous media. Numerical simulations show that this imaging method is quite effective because it masks the strong specular reflections from the bulk of the object to be imaged, allowing us to image the edges. It is also robust to noise if the array has a large number of sensors. In the Fraunhofer regime the analysis of selective subspace migration imaging can be carried out using the theory of generalized prolate spheroidal wave functions. Imaging extended reflectors with ultrasound is

[2]The result in [29] holds for other regions of $\mathbb{C}$ not containing the origin.

not, however, in the Fraunhofer regime but rather in an extended one. The theory of generalized prolate spheroidal wave functions carries over only partially into the extended Fraunhofer regime. This is enough, however, to explain much of what we see in the numerical simulations.

There are many things that are not addressed here, but should be. On the theoretical side is developing a more complete theory for imaging in the extended Fraunhofer regime and with nonconstant reflectivities. On the side of applications as well as theory are questions about robustness to noise and sensor sparsity that need a deeper analysis. Extensions to random media and optimal subspace selection and illumination, as in [4], also need to be considered.

Appendix A. Rectangular array and target. For a rectangular array $\mathcal{A}$ and target $\mathcal{B}$, centered at the origin, the eigenvalues and eigenfunctions of the space and wavenumber limiting operator $\mathcal{A}Q_{\frac{k}{L}\mathcal{B}}\mathcal{A}$ can be expressed in terms of the prolate spheroidal wave functions [42, 30, 41]. The eigenvalue distribution of $\mathcal{A}Q_{\frac{k}{L}\mathcal{B}}\mathcal{A}$ for such $\mathcal{A}$ and $\mathcal{B}$ can also be inferred from existing one-dimensional results [31].

A.1. The one-dimensional prolate spheroidal wave functions. Slepian and Pollak [42] found the eigenfunctions and eigenvalues of the one-dimensional space and wavenumber limiting (called time and band limiting in [42]) operator $\mathcal{P}[C] = P_{[-1,1]}Q_{[-C,C]}P_{[-1,1]}$ with kernel representation,

$$(\mathcal{P}[C]f)(x) = \int_{-1}^{1} dy f(y) \frac{\sin[C(x-y)]}{\pi(x-y)}. \tag{A.1}$$

Here $P_{[-1,1]}$ is the orthogonal projection that restricts functions to the interval $[-1,1]$, and $Q_{[-C,C]} = \mathcal{F}^{-1}P_{[-C,C]}\mathcal{F}$ restricts a function to $[-C,C]$ in the Fourier domain. The elegant method of Slepian and Pollak consists in showing that the operator $\mathcal{P}[C]$ commutes with a differential operator for which the eigenfunctions are known explicitly [1, section 21]. The eigenvalues of $\mathcal{P}[C]$ are denoted by $\nu_n(C)$ (in decreasing order) and its eigenfunctions $\psi_n(x;C)$, with normalization $\|\psi_n(\cdot;C)\|^2_{L^2[-1,1]} = \nu_n(C)$. Since the operator $\mathcal{P}[C]$ is positive and Hermitian, the singular values and singular functions are the eigenvalues and eigenfunctions.

The first order asymptotic for the eigenvalue distribution (the one-dimensional analogue of (4.13)) is that, except for relatively few eigenvalues, the first $n^*(C) = \lfloor 2C/\pi \rfloor$ eigenvalues are asymptotically close to one, and the rest approach zero as the dilation factor $C \to \infty$ (see, e.g., [40]).

A.2. Eigenvalues and eigenfunctions. Finding the eigenvalues of the operator $\mathcal{A}Q_{\mathcal{B}}\mathcal{A}$ when $\mathcal{A} = \prod_{i=1}^{2}[-a_i/2, a_i/2]$ and $\mathcal{B} = \prod_{i=1}^{2}[-b_i/2, b_i/2]$ in terms of the prolate spheroidal wave functions is done with separation of variables and change of integration variables. For simplicity, we drop in this section the dilation factor k/L and suppose that $\mathcal{B}$ already includes it.

Proposition A.1. *For rectangular sets*

$$\mathcal{A} = \prod_{i=1}^{2}[-a_i/2, a_i/2] \quad \textit{and} \quad \mathcal{B} = \prod_{i=1}^{2}[-b_i/2, b_i/2]$$

the (unsorted) eigenvalues and eigenfunctions of $\mathcal{A}Q_{\mathcal{B}}\mathcal{A}$ *are, for* $\mathbf{x} = (x_1, x_2) \in \mathcal{A}$,

$$\sigma_{\mathbf{n}}[\mathcal{A}Q_{\mathcal{B}}\mathcal{A}] = \prod_{i=1}^{2} \nu_{n_i}\left(\frac{a_i b_i}{4}\right) \quad \textit{and} \quad v_{\mathbf{n}}[\mathcal{A}Q_{\mathcal{B}}\mathcal{A}](\mathbf{x}) \sim \prod_{i=1}^{2} \psi_{n_i}\left(\frac{2}{a_i}x_i; \frac{a_i b_i}{4}\right),$$

where the symbol $\sim$ *means equality up to a norming constant and* $\mathbf{n} = (n_1, n_2) \in \mathbb{N}^2$. *For the "dual" operator* $\mathcal{B}Q^*_{\mathcal{A}}\mathcal{B}$ *we have* $\sigma_{\mathbf{n}}[\mathcal{B}Q^*_{\mathcal{A}}\mathcal{B}] = \sigma_{\mathbf{n}}[\mathcal{A}Q_{\mathcal{B}}\mathcal{A}]$, *with eigenfunctions*

$$v_{\mathbf{n}}[\mathcal{B}Q^*_{\mathcal{A}}\mathcal{B}](\mathbf{y}) \sim \prod_{i=1}^{2} \psi_{n_i}\left(\frac{2}{b_i}y_i; \frac{a_i b_i}{4}\right) \quad \textit{for} \quad \mathbf{y} = (y_1, y_2) \in \mathcal{B}.$$

That the eigenfunctions of the "dual" operator $\mathcal{B}Q^*_{\mathcal{A}}\mathcal{B}$ are the prolate spheroidal wave functions stretched to $\mathcal{B}$ is a manifestation of the self-similarity under Fourier transform of the prolate spheroidal wave functions [41].

The staircase aspect of the eigenvalues of $\mathcal{A}Q_{\mathcal{B}}\mathcal{A}$ for a rectangular array and target can be explained qualitatively by Proposition A.1 and by the characteristic plateau behavior of $\nu_n(C)$. Roughly speaking, each eigenvalue $\nu_{n_1}(a_1b_1/4)$ that is in the plunge region for $\mathcal{P}[a_1b_1/4]$ has multiplicity $n^*(a_2b_2/4)$ as an eigenvalue of $\mathcal{A}Q_{\mathcal{B}}\mathcal{A}$, since $\prod_{i=1}^{2} \nu_{n_i}(a_ib_i/4) \approx \nu_{n_1}(a_1b_1)$ for $n_2 \leq n^*(a_2b_2/4)$.

We show in Figure 15 some of the eigenfunctions of $\mathcal{P}[a_ib_i/4]$ for dimensions $a_i = 24.5\lambda_0$ and $b_i = (k_0/L)20\lambda_0 = 2\pi/(5\lambda_0)$, taken from the setup of section 3. The eigenfunctions up to $n^*(a_ib_i/4) = 4.9$ are well localized in $[-a/2, a/2]$, but then spill outside this interval. The eigenfunctions of $\mathcal{P}[a_ib_i/4]$ that are better localized on the edges of the array are near the threshold $n^*(a_ib_i/4)$. We recall that the extension of the domain of definition of the singular functions is done with (4.15).

The eigenfunctions we use as illuminations in our method are mostly localized on the edges of $\mathcal{A}$. Moreover, the associated eigenfunctions on the target side are also localized near the edges of $\mathcal{B}$. Thus, by Proposition 4.5 the images concentrate near the edges of $\mathcal{B}$ in the Fraunhofer regime.

However, the behavior of the array response matrix is better described in the extended Fraunhofer regime, as we saw in Figure 14. Thus, for comparison we include in Figure 15 some of the eigenfunctions of the one-dimensional operator (5.2) that appears in the extended Fraunhofer regime array response matrix for a rectangular array and target. We see that, at least on the array side, the eigenfunctions are localized, but that they spill over faster outside the array. As for the eigenvalues, they also decay faster than those in the usual Fraunhofer regime. The extension of the eigenfunctions was done similarly to (4.15). The study of the operator (5.2) and the characterization of images in the extended Fraunhofer regime are left for future studies.

A.3. Eigenvalue distribution. We show that for rectangular sets $\mathcal{A}$ and $\mathcal{B}$ in space and Fourier domain, the eigenvalue distribution of $\mathcal{A}Q_{\frac{k}{L}\mathcal{B}}\mathcal{A}$ is consistent with that conjectured by Widom (4.14). This is based on the two-term asymptotic distribution for $\mathcal{P}[C]$ due to Landau and Widom [31], and we formulate it as a large Fresnel number $\theta_{ab} = kab/L$ asymptotic in the following proposition.

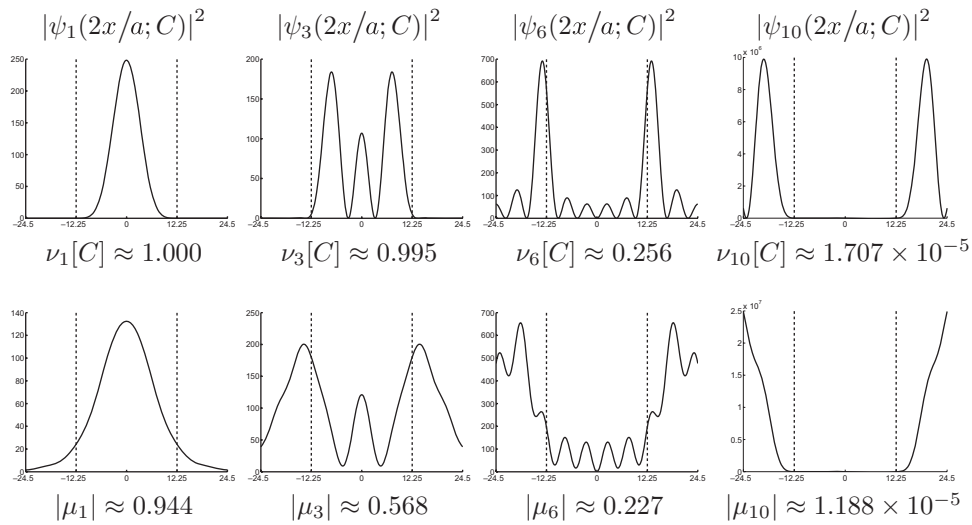

Figure 15. *Top row: some eigenfunctions of $\mathcal{P}[C]$ stretched to $[-a/2, a/2]$ with $C = 49\pi/20$. Bottom row: some eigenfunctions of the operator (5.2), ordered by decreasing magnitude of the associated eigenvalues μ_n. The eigenfunctions are consistent with the setup in section 3 at the central frequency, that is, $k = 2\pi/\lambda_0$, $L = 100\lambda_0$, $a = 24.5\lambda_0$, and $b = 20\lambda_0$. The abscissa $-a/2$ and $a/2$ are in dotted lines, with units λ_0. The functions are rescaled to have unit $L^2([-a/2, a/2])$ norm and are extended to $[-a, a]$.*

Proposition A.2. *For rectangular sets*

$$\mathcal{A} = \prod_{i=1}^{2}[-a_i/2, a_i/2] \quad \text{and} \quad \mathcal{B} = \prod_{i=1}^{2}[-b_i/2, b_i/2],$$

with respective length scales a and b, the eigenvalue distribution of $\mathcal{A}Q_{\frac{k}{L}\mathcal{B}}\mathcal{A}$ is consistent with the Widom conjecture (4.14): as $\theta_{ab} = kab/L \to \infty$ we have

$$N(\delta;\theta_{ab}) = (\lambda L)^{-2}a_1a_2b_1b_2 + (\lambda L)^{-1}\frac{\ln\theta_{ab}}{4\pi^2}4(a_1b_1 + a_2b_2)\ln\frac{1-\delta}{\delta} + o(\theta_{ab}\ln\theta_{ab}).$$

Proof. By Proposition A.1, we have $\sigma_{\mathbf{n}}[\mathcal{A}Q_{\frac{k}{L}\mathcal{B}}\mathcal{A}] = \nu_{n_1}(C_1)\nu_{n_2}(C_2)$ for $(n_1, n_2) \in \mathbb{N}^2$ with

$$C_i = \frac{ka_ib_i}{4L}, \quad i = 1, 2,$$

and where $\nu_{n_i}(C_i)$ are the eigenvalues of the operator $\mathcal{P}[C_i]$ (recall (A.1)). Using the asymptotic expansion of Landau and Widom [31] (see also [41]) of the eigenvalue distribution of $\mathcal{P}[C]$, we obtain, for large Fresnel number θ_{ab},

$$N^{(i)}(\delta;\theta_{ab}) = (\lambda L)^{-1}a_ib_i + \frac{1}{\pi^2}\ln(\theta_{ab})\ln\frac{1-\delta}{\delta} + o(\ln\theta_{ab}), \tag{A.2}$$

where $N^{(i)}(\delta;\theta_{ab}) = \#\{n|\nu_n(C_i) > \delta\}$ and $i = 1, 2$. Notice that

$$\begin{aligned} N(\delta;\theta_{ab}) &= \#\left\{\mathbf{n} = (n_1, n_2) \in \mathbb{N}^2 \mid \sigma_{\mathbf{n}}[\mathcal{A}Q_{\frac{k}{L}\mathcal{B}}\mathcal{A}] = \nu_{n_1}(C_1)\nu_{n_2}(C_2) > \delta\right\} \\ &= \sum_{n_1=1}^{\infty} \#\left\{n_2 \mid \nu_{n_2}(C_2) > \frac{\delta}{\nu_{n_1}(C_1)}\right\} = \sum_{n_1=1}^{\infty} N^{(2)}\left(\frac{\delta}{\nu_{n_1}(C_1)};\theta_{ab}\right), \end{aligned}$$

where we can divide by $\nu_{n_1}(C_1)$ because the operator $\mathcal{P}[C]$ is positive. But we have $\delta \geq \nu_{n_1}(C_1)$ for $n_1 > N^{(1)}(\delta;\theta_{ab})$ and $N^{(2)}(\alpha;\theta_{ab}) = 0$ for $\alpha \geq 1$, so it is easy to see that the above sum has only a few nonzero terms, giving

$$N(\delta;\theta_{ab}) = \sum_{n_1=1}^{N^{(1)}(\delta;\theta_{ab})} N^{(2)}\left(\frac{\delta}{\nu_{n_1}(C_1)};\theta_{ab}\right).$$

For most $n_1 \leq N^{(1)}(\delta;\theta_{ab})$, we have that $\nu_{n_1}(C_1) \to 1$ as $\theta_{ab} \to \infty$, with only a few $o(\theta_{ab})$ exceptions where the limit of $\nu_{n_1}(C_1)$ is not one, which happens when n_1 nears $N^{(1)}(\delta;\theta_{ab})$. This observation together with the asymptotics (A.2) of the summand gives $N(\delta;\theta_{ab}) = N^{(1)}(\delta;\theta_{ab})N^{(2)}(\delta;\theta_{ab}) + N^{(1)}(\delta;\theta_{ab})o(\ln\theta_{ab})$. The result follows from (A.2). ■

A.4. Eigenvalue computation. The downside of Proposition A.1 is that it does not give any information about the ordering of the eigenvalues. Fortunately, we are interested only in the eigenvalues of $\mathcal{A}Q_{\frac{k}{L}\mathcal{B}}\mathcal{A}$ that are for practical purposes nonzero.

According to Proposition A.2, and for large enough θ_{ab}, the number $N(\delta;\theta_{ab})$ of eigenvalues of $\mathcal{A}Q_{\frac{k}{L}\mathcal{B}}\mathcal{A}$ above some $0 < \delta < 1$ is essentially $\prod_{i=1}^{2} N^{(i)}(\delta;\theta_{ab})$, where $N^{(i)}(\delta;\theta_{ab})$ is the number of eigenvalues above δ of $\mathcal{P}[ka_ib_i/(4L)]$. Thus to find the singular values above some δ, we compute $\sigma_{\mathbf{n}}[\mathcal{A}Q_{\frac{k}{L}\mathcal{B}}\mathcal{A}]$ for $\mathbf{n} \in \mathbb{N}^2 \cap \prod_{i=1}^{2}[1, N^{(i)}(\delta;\theta_{ab})]$ and then sort them in decreasing order.

For the eigenvalues of $\mathcal{A}Q_{\frac{k}{L}\mathcal{B}}\mathcal{A}$ in Figure 14, we computed the first 100 eigenvalues of $\mathcal{P}[ka_ib_i/(4L)]$, which is well into the region where the $\nu_n(ka_ib_i/(4L))$ are almost zero. This gives 10^4 unsorted eigenvalues for $\mathcal{A}Q_{\frac{k}{L}\mathcal{B}}\mathcal{A}$. We sort them and keep the 100 largest ones.

Appendix B. Other computational issues. Computations for the forward problem were done with the Born approximation (3.1), which can be seen as a symmetric matrix-matrix multiplication if the sources and receivers are collocated in the array. This is a so-called level-3 linear algebra operation that can achieve near peak processor performance when using tuned BLAS libraries such as ATLAS or the Intel MKL.

A significant part of the computational cost of our method is spent computing the SVD of the array response matrix, especially for the 50×50 array where the array response matrix is $\mathbb{C}^{2500\times 2500}$. This is an embarrassingly parallel task, since it can be done independently frequency by frequency. However, we did not parallelize the SVD computations in our code. Instead we noted that the Fraunhofer regime theory of section 4.1 predicts that the array response matrix is effectively low-rank, and that its rank can be estimated a priori by having an idea of the area of the target.

Therefore we need only compute the first few singular vectors and values of the array response matrix, and this can be done efficiently using an iterative method. We use the

MATLAB `eigs` interface to ARPACK [32]. The low rank of the response matrix can also be used to reduce the storage of the frequency samples. In our computations, we store only the first 100 singular vectors and values of the data, which is the best rank-100 approximation in the matrix 2 norm and Frobenius norm; see, e.g. [20, section 2.5.5]. This was enough to capture the significantly nonzero singular values. Of course, when we add noise to the array response matrix we add it before such compression.

The imaging method described in section 2.2 uses only the intermediate singular values, which are a relatively small part of the data. It would be interesting to directly compute the singular vectors corresponding to intermediate singular values. In principle a simple spectral transformation can make the intermediate singular values the ones with largest magnitude, for example, the transformation $A(\sigma_1[A]I - A)$, where $A = \widehat{\Pi}^*(\omega)\widehat{\Pi}(\omega)$.

Appendix C. The full aperture problem. We consider here the full aperture scattering problem for a disk-shaped reflector of radius b, in two dimensions, in order to show how the ideas in the paper extend to this case. The full aperture data have the form

$$\widehat{\Pi}(\vec{\mathbf{x}}_r, \vec{\mathbf{x}}_s, \omega) = \frac{e^{2ikR}}{R^2}\mathcal{S}_\omega(\vec{\theta}_r, \vec{\theta}_s), \tag{C.1}$$

where the sources and receivers are on a disk of radius $R \gg b$, concentric with the reflector, and $k = \omega/c_0$. We have

$$\vec{\mathbf{x}}_r = R\vec{\theta}_r, \quad \vec{\mathbf{x}}_s = R\vec{\theta}_s$$

for unit vectors[3]

$$\vec{\theta}_r = (\cos\theta_r, \sin\theta_r), \quad \vec{\theta}_s = (\cos\theta_s, \sin\theta_s).$$

With the Born approximation, the kernel of the far field operator is

$$\mathcal{S}_\omega(\vec{\theta}_r, \vec{\theta}_s) = \frac{k^2}{(4\pi)^2}\widehat{\rho}\left(k\vec{\theta}_r + k\vec{\theta}_s\right), \tag{C.2}$$

as follows easily from the far field approximation of the Green's function

$$\widehat{G}_0(\vec{\mathbf{x}}, \vec{\mathbf{y}}, \omega) \approx \frac{e^{ikR}}{4\pi R}e^{-ik\vec{\theta}\cdot\vec{\mathbf{y}}} \tag{C.3}$$

for $\vec{\mathbf{x}} = R\vec{\theta}$ and $\vec{\mathbf{y}}$ a point in the reflector ($|\vec{\mathbf{y}}| \le b$). Thus, the SVD analysis of $\widehat{\Pi}(\omega)$ reduces to the analysis of the operator with kernel $\widehat{\rho}(k\vec{\theta}_r + k\vec{\theta}_s)$.

The singular values (see [27, 28]) have the form

$$\mu_n = \int_0^b J_n^2(kr)r\,dr, \tag{C.4}$$

where J_n is the Bessel function of order n. The right singular functions of the far field operator are given by

$$v_n(\theta_s) = \cos(n\theta_s) \quad \text{or} \quad \sin(n\theta_s), \tag{C.5}$$

[3]The notation θ_r for angles should not be confused with that for Fresnel numbers (section 4.1).

and, using (C.1) and (C.2), we get the singular vectors of $\widehat{\Pi}(\omega)$

$$V_n(\theta_s) = \frac{e^{-ikR}}{4\pi R} v_n(\theta_s) \approx \overline{\widehat{G}_0(\vec{\mathbf{x}}_s, \vec{0}, \omega)} v_n(\theta_s). \tag{C.6}$$

It follows from the properties of the Bessel functions [1, Chapter 9] that the singular values are uniformly large for indices $n < kb$ and then plunge to zero for $n > kb$. Thus, the threshold is

$$N^*(\omega) = [kb], \tag{C.7}$$

as obtained in [27, 28]. What we wish to show here is that when we illuminate the reflector with the transition singular vectors $V_{N^*}(\theta_s)$, we obtain images that are focused on the edges of the disk.

The single frequency migration image is

$$\mathcal{J}(\vec{\mathbf{y}}^S, \omega, n) = \int_0^{2\pi} d\theta_r \left[\int_0^{2\pi} d\theta_s \overline{\widehat{\Pi}(\vec{\mathbf{x}}_r, \vec{\mathbf{x}}_s, \omega) V_n(\theta_s)} \right] \widehat{G}_0(\vec{\mathbf{x}}_r, \vec{\mathbf{y}}^S, \omega). \tag{C.8}$$

Since

$$\left[\widehat{\Pi}(\omega) V_n \right] (\theta_r) \sim \mu_n \overline{V_n(\theta_r)}, \tag{C.9}$$

we have

$$\mathcal{J}(\vec{\mathbf{y}}^S, \omega, n) \sim \mu_n \int_0^{2\pi} d\theta_r V_n(\theta_r) \widehat{G}_0(\vec{\mathbf{x}}_r, \vec{\mathbf{y}}^S, \omega) \approx \mu_n \int_0^{2\pi} d\theta_r \overline{v_n(\theta_r)} e^{-ikr^S \cos(\theta_r - \varphi^S)}.$$

Here we used the polar coordinates

$$\vec{\mathbf{y}}^S = r^S \left(\cos\varphi^S, \sin\varphi^S \right).$$

Using (C.5) we get the single frequency image

$$\mathcal{J}(\vec{\mathbf{y}}^S, \omega, n) \sim \mu_n e^{in\varphi^S} J_n(kr^S). \tag{C.10}$$

We plot $\mathcal{J}(\vec{\mathbf{y}}^S, \omega, n)/\mu_n$ in Figure 16 for $kb = 100$ and for $kb = 110$. Note how it peaks at $r^S = 0$ when we use the leading singular vectors V_0, and how the peaks move to the boundary of the disk when we use the transition singular vectors $V_{N^\star}$. The images are greatly improved when we integrate over the bandwidth $kb \in [100, 200]$, as shown in Figure 16. This is because the oscillations of the Bessel functions cancel out in the integration. In particular, the image

$$\mathcal{J}(\vec{\mathbf{y}}^S) = \int d\omega \mathcal{J}\left(\vec{\mathbf{y}}^S, \omega, N^\star(\omega)\right) \tag{C.11}$$

is nicely focused on the edges of the reflector.

Acknowledgment. The authors would like to thank the anonymous referees for their helpful remarks and especially for referring us to the related work by Kusiak and Sylvester [27, 28], Haddar, Kusiak, and Sylvester [22], Colton and Kress [14], and Colton, Coyle, and Monk [11].

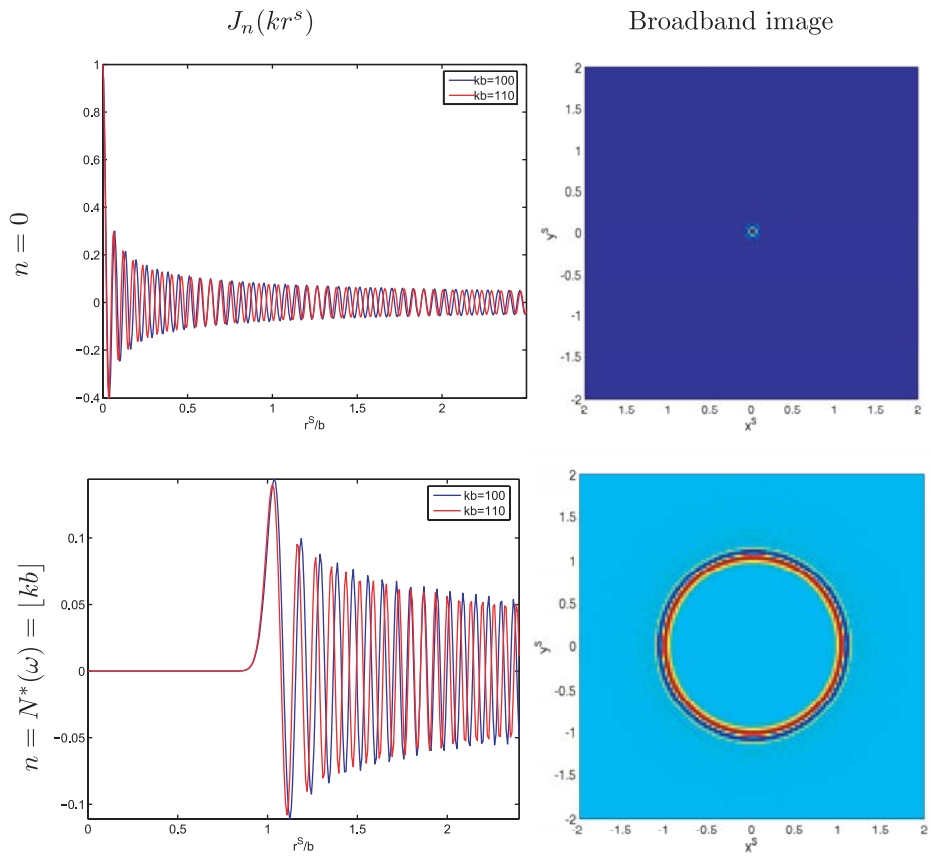

Figure 16. *Left: we plot the normalized single frequency image versus* $r^S = |\vec{\mathbf{y}}^S|$. *We show two images, for* $kb = 100$ *and* $kb = 110$. *Right: we plot the broadband image. The top line is for illuminations with the leading singular vectors and the bottom line is for illuminations with the transition singular vectors.*

REFERENCES

[1] M. Abramowitz and I. A. Stegun, eds., *Handbook of Mathematical Functions*, Appl. Math. Ser., National Bureau of Standards, Washington, D.C., 1964.

[2] B. L. Biondi, 3D *Seismic Imaging*, Investigations in Geophysics 14, Society of Exploration Geophysicists, Tulsa, OK, 2006.

[3] N. Bleistein, J. K. Cohen, and J. W. Stockwell, Jr., *Mathematics of Multidimensional Seismic Imaging, Migration, and Inversion*, Interdiscip. Appl. Math. 13, Geophysics and Planetary Sciences, Springer-Verlag, New York, 2001.

[4] L. Borcea, G. Papanicolaou, and C. Tsogka, *Optimal illumination and waveform design for imaging in random media*, J. Acoust. Soc. Amer., 122 (2007), pp. 3507–3518.

[5] L. Borcea, G. Papanicolaou, and C. Tsogka, *Optimal waveform design for array imaging*, Inverse Problems, 23 (2007), pp. 1973–2020.

[6] L. Borcea, G. Papanicolaou, C. Tsogka, and J. Berryman, *Imaging and time reversal in random media*, Inverse Problems, 18 (2002), pp. 1247–1279.

[7] B. Borden, *Mathematical problems in radar inverse scattering*, Inverse Problems, 19 (2002), pp. R1–R28.

[8] M. Born and E. Wolf, *Principles of Optics: Electromagnetic Theory of Propagation, Interference and Diffraction of Light*, 7th ed., Cambridge University Press, Cambridge, UK, 1999.

[9] J. Claerblout and S. Doherty, *Downward continuation of moveout-corrected seismograms*, Geophysics, 37 (1972), pp. 741–768.

[10] J. F. Claerbout, *Imaging the Earth's Interior*, Blackwell, Oxford, UK, 1985.

[11] D. Colton, J. Coyle, and P. Monk, *Recent developments in inverse acoustic scattering theory*, SIAM Rev., 42 (2000), pp. 369–414.

[12] D. Colton, H. Haddar, and M. Piana, *The linear sampling method in inverse electromagnetic scattering theory*, Inverse Problems, 19 (2003), pp. S106–S137.

[13] D. Colton and A. Kirsch, *A simple method for solving inverse scattering problems in the resonance region*, Inverse Problems, 12 (1996), pp. 383–393.

[14] D. Colton and R. Kress, *Inverse Acoustic and Electromagnetic Scattering Theory*, Appl. Math. Sci. 93, Springer-Verlag, Berlin, 1998.

[15] J. Curlander and R. McDonough, *Synthetic Aperture Radar*, Wiley, New York, 1991.

[16] O. Dorn and D. Lesselier, *Level set methods for inverse scattering*, Inverse Problems, 22 (2006), pp. R67–R131.

[17] A. Edelman, *Eigenvalues and Condition Numbers of Random Matrices*, Ph.D. thesis, Massachusetts Institute of Technology, Cambridge, MA, 1989.

[18] S. Geman, *A limit theorem for the norm of random matrices*, Ann. Probab., 8 (1980), pp. 252–261.

[19] D. Gioev, *Szegő limit theorem for operators with discontinuous symbols and applications to entanglement entropy*, Int. Math. Res. Not., 2006 (2006), article ID 95181.

[20] G. H. Golub and C. F. Van Loan, *Matrix Computations*, 3rd ed., Johns Hopkins Series in the Mathematical Sciences, The Johns Hopkins University Press, Baltimore, MD, 1996.

[21] B. B. Guzina and M. Bonnet, *Topological derivative for the inverse scattering of elastic waves*, Quart. J. Mech. Appl. Math., 57 (2004), pp. 161–179.

[22] H. Haddar, S. Kusiak, and J. Sylvester, *The convex back-scattering support*, SIAM J. Appl. Math., 66 (2005), pp. 591–615.

[23] E. M. Hyde and O. P. Bruno, *A fast, higher-order solver for scattering by penetrable bodies in three dimensions*, J. Comput. Phys., 202 (2005), pp. 236–261.

[24] M. Kac, W. L. Murdock, and G. Szegő, *On the eigenvalues of certain Hermitian forms*, J. Ration. Mech. Anal., 2 (1953), pp. 767–800.

[25] N. J. Kasdin, R. J. Vanderbei, M. G. Littman, and D. N. Spergel, *Optimal one-dimensional apodizations and shaped pupils for planet finding coronagraphy*, Appl. Opt., 44 (2005), pp. 1117–1128.

[26] S. Komilikis, C. Prada, and M. Fink, *Characterization of extended objects with the D.O.R.T. method*, in Proceedings of the 1996 IEEE Ultrasonics Symposium, Vol. 2, 1996, pp. 1401–1404.

[27] S. Kusiak and J. Sylvester, *The scattering support*, Commun. Pure Appl. Math., 56 (2003), pp. 1525–1548.

[28] S. Kusiak and J. Sylvester, *The convex scattering support in a background medium*, SIAM J. Math. Anal., 36 (2005), pp. 1142–1158.

[29] H. J. Landau, *On Szegő's eigenvalue distribution theorem and non-Hermitian kernels*, J. Anal. Math., 28 (1975), pp. 335–357.

[30] H. J. Landau and H. O. Pollak, *Prolate spheroidal wave functions, Fourier analysis and uncertainty.* II, Bell System Tech. J., 40 (1961), pp. 65–84.

[31] H. J. Landau and H. Widom, *Eigenvalue distribution of time and frequency limiting*, J. Math. Anal. Appl., 77 (1980), pp. 469–481.

[32] R. B. Lehoucq, D. C. Sorensen, and C. Yang, *ARPACK Users' Guide: Solution of Large-Scale Eigenvalue Problems with Implicitly Restarted Arnoldi Methods*, Software Environ. Tools 6, SIAM, Philadelphia, PA, 1998.

[33] F. Lin, A. I. Nachman, and R. C. Waag, *Quantitative imaging using a time-domain eigenfunction method*, J. Acoust. Soc. Am., 108 (2000), pp. 899–912.

[34] R. Marklein, K. J. Langenberg, K. Mayer, J. Miao, A. Shilivinski, A. Zimmer, W. Müller, V. Schmitz, C. Kohl, and U. Mletzko, *Recent applications and advances of numerical modeling and wavefield inversion in nondestructive testing*, Adv. Radio Sci., 3 (2005), pp. 167–174.

[35] T. Mast, A. I. Nachman, and R. Waag, *Focusing and imaging using eigenfunctions of the scattering operator*, J. Acoust. Soc. Am., 102 (1997), pp. 715–725.

[36] C. Prada and M. Fink, *Eigenmodes of the time reversal operator: A solution to selective focusing in multiple-target media*, Wave Motion, 20 (1994), pp. 151–163.

[37] F. Santosa, *A level set approach for inverse problems involving obstacles*, ESAIM Control Optim. Calc. Var., 1 (1996), pp. 17–33.

[38] D. Slepian, *Prolate spheroidal wave functions, Fourier analysis and uncertainty.* IV. *Extensions to many dimensions; generalized prolate spheroidal functions*, Bell System Tech. J., 43 (1964), pp. 3009–3057.

[39] D. Slepian, *Analytic solution of two apodization problems*, J. Opt. Soc. Amer., 55 (1965), pp. 1110–1115.

[40] D. Slepian, *On bandwidth*, Proc. IEEE, 64 (1976), pp. 292–300.

[41] D. Slepian, *Some comments on Fourier analysis, uncertainty and modeling*, SIAM Rev., 25 (1983), pp. 379–393.

[42] D. Slepian and H. O. Pollak, *Prolate spheroidal wave functions, Fourier analysis and uncertainty.* I, Bell System Tech. J., 40 (1961), pp. 43–63.

[43] M. Tanter, J.-F. Aubry, J. Gerber, J.-L. Thomas, and M. Fink, *Optimal focusing by spatio-temporal inverse filter.* I. *Basic principles*, J. Acoust. Soc. Am., 110 (2001), pp. 37–47.

[44] M. Tanter, J.-L. Thomas, and M. Fink, *Time reversal and the inverse filter*, J. Acoust. Soc. Am., 108 (2000), pp. 223–234.

[45] L. N. Trefethen and M. Embree, *Spectra and Pseudospectra. The Behavior of Nonnormal Matrices and Operators*, Princeton University Press, Princeton, NJ, 2005.

[46] C. R. Vogel, *Computational Methods for Inverse Problems*, Frontiers Appl. Math., SIAM, Philadelphia, PA, 2002.

[47] H. Widom, *A theorem on translation kernels in n dimensions*, Trans. Amer. Math. Soc., 94 (1960), pp. 170–180.

[48] H. Widom, *Asymptotic inversion of convolution operators*, Inst. Hautes Étud. Sci. Publ. Math., 44 (1974), pp. 191–240.

[49] H. Widom, *On a class of integral operators with discontinuous symbol*, in Toeplitz Centennial (Tel Aviv, 1981), Oper. Theory Adv. Appl. 4, Birkhäuser, Basel, 1982, pp. 477–500.

[50] H. Widom, *On a class of integral operators on a half-space with discontinuous symbol*, J. Funct. Anal., 88 (1990), pp. 166–193.

[51] K. Yosida, *Functional Analysis*, Classics Math., 6th ed., Springer-Verlag, Berlin, 1980.